Chapter 15
Penetration Investigations in Lunar Regolith and Simulants

Jared Atkinson

Abstract The American Apollo and Soviet Luna missions to the Moon during the 'space race' led to a vast collection of knowledge regarding the properties of the lunar surface. A critical but often under-appreciated investigative tool used in the missions is the penetrometer, a simple device which was successfully operated both manually and semi-autonomously to penetrate and characterize the unknown lunar regolith. Since that time, penetrometers have seen little use in investigations of returned lunar soil (also called regolith) or—more often—regolith simulants, though a few intrepid researchers have continued using the penetrometer in various forms. Recent work provides evidence that both the penetration and relaxation behavior of the regolith can help to determine useful physical properties, including important indications of ice content, cohesion, and particle angularity. Current plans to return to the Moon's polar regions to explore icy regolith are being developed along with in-situ resource utilization (ISRU) demonstration missions, and some will likely include instruments for determining in-situ regolith properties using penetrometer technology.

15.1 Introduction

The American Apollo and Soviet Luna missions to the Moon during the space race led to a vast collection of knowledge regarding the properties of the lunar surface. A critical but often under-appreciated investigative tool used in the missions is the penetrometer, a simple device which was successfully operated both manually and semi-autonomously to penetrate and characterize the unknown lunar regolith. Since that time, penetrometers have seen little use in investigations of returned lunar soil (also called regolith) or—more often—regolith simulants, though a few intrepid researchers have continued using the penetrometer in various forms. Recent work provides evidence that both the penetration and relaxation behavior of the regolith can help to determine useful physical properties, including important indications of ice content, cohesion, and particle angularity.

J. Atkinson (✉)
Honeybee Robotics, 2408 Lincoln Ave., Altadena, CA 91001, USA
e-mail: jwgatkin@alum.mit.edu

V. Badescu et al. (eds.), *Handbook of Space Resources*,
https://doi.org/10.1007/978-3-030-97913-3_15

Plans to return to the Moon's polar regions to explore icy regolith are currently in development some of which will include instruments for determining in-situ regolith properties using the technology and techniques discussed in this chapter. The discussion will start with a brief description of the penetrometer and the physical mechanisms involved in soil penetration and relaxation, followed by a brief history of lunar penetrometer investigations and the subsequently developed lunar simulants. The chapter will end with a review of the more pertinent and interesting research using penetrometers in regolith and their simulants since those first (and last) steps onto the lunar surface over half a century ago.

15.2 Penetrometer History, Measurements, and Applications

15.2.1 Introduction

A penetrometer can be thought of as any sort of rigid object—generally rod-like—that is pushed into a material to derive some sort of qualitative or quantitative measurement of its firmness, hardness, compaction, or strength. The earliest penetrometers were fists and thumbs, fingernails, sticks, and metal rods (Kirkham 2014), for millennia used to determine the consistency of a mixture, the strength of mud for building shelter, or the safety of the ground beneath an explorer's feet in a soggy wetland. The basic idea is this: the firmer or more solid the material, the more it *resists* penetration. As it turns out, the actual mechanics of penetration are more complicated than one would expect, and researchers have devoted entire careers to understanding the physics of how soils and other materials deform under penetration, and what that deformation can tell us about the material's fundamental properties.

Modern field penetrometers are generally metal rods (Sanglerat 1972) connected to a force-measuring device (electronic sensor, proving ring, etc.), pushed into a medium at a specified rate, that determine the resistance to vertical penetration with depth. The quantitative measurement of resistance is then correlated to soil characteristics (Kirkham 2014) such as bearing capacity, safe soil pressure, rolling resistance, wheel trafficability, relative density, crop yields, and a whole host of other—typically non-fundamental—properties. New research, however, aims at correlating the penetration resistance and subsequent relaxation to more fundamental soil properties (Oravec et al. 2010; Cil 2011; Atkinson et al. 2019, 2020).

Penetrometers used in the field exist in two main forms: portable hand-operated (Fig. 15.1), or machine-operated and stationary (Blok et al. 2019). Those used in laboratory testing have often been manually operated (and consequently prone to user error), while newer studies tend to focus on controlled mechanisms that limit lateral motion, maintain consistent penetration rates, and record penetration resistance continuously during operation (e.g., Atkinson et al. 2019). Two types of penetration tests also exist: static and dynamic (Kirkham 2014). Static tests consist of a

Fig. 15.1 A standard field penetrometer. *Source* Kirkham (2014)

penetrometer pushed steadily into the soil, such as the traditional cone penetration test (CPT) (Lunne et al. 1997), while dynamic tests involve a penetrometer driven into the soil by a hammer or falling weight resulting in a direct measurement of depth per blow rather than resistance as a function of depth.

15.2.2 History

While humanity has used rod-like tools to probe the ground far before the first recorded instance, the method of measuring the strength of sub-surface soil using a rod has been attributed to French researchers (1846), who used a 1-mm diameter needle and 1-kg weight to probe clays of various consistencies and estimate the resulting cohesion (Sanglerat 1972). A comprehensive review of the penetrometer history is given by Sanglerat (1972) and an excellent overview by Lunne et al. (1997).

The invention of the modern cone penetrometer, arguably the most widely used device for field determinations of soil properties, is alternatively attributed to the US Army Corps of Engineers in the early 1940s (Oravec 2009; Kirkham 2014) and to the Dutch in the 1930s (Lunne et al. 1997). The Dutch cone penetrometer was developed in the Laboratory for Soil Mechanics at Delft University of Technology. It had a base area of 10 cm^2 and an apex angle of 60° (Durgunoglu and Mitchell 1973), and the first tests were conducted in 1932 (Lunne et al. 1997). The US version was developed at the Waterways Experiment Station during WWII and was composed of a 1.59-cm diameter rod, a proving ring with dial gage (for measuring force), a cone tip of 30°, and a 323-mm^2 base area (Fig. 15.2) (Oravec 2009, and citations within). Originally intended to predict the carrying capacity of fine-grained soils for off-road military vehicles, it provided a single value (Bekker 1969) that combined mechanical soil properties (such as soil drag and thrust) into one convenient parameter that could be interrelated with soil trafficability—a particularly important measurement in “go/no-go” analyses for military vehicles.

Concurrently, the electronic penetrometer—providing nearly continuous and sensitive penetration data—was developed in Berlin during WWII and has become a

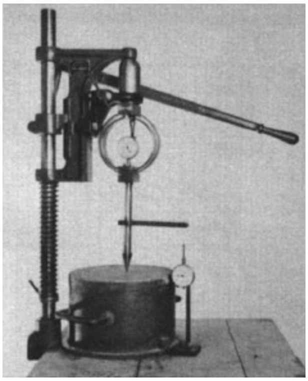

Fig. 15.2 Army Corps of Engineers original laboratory cone penetrometer. Right: Typical field penetrometer. *Source* Department of the Army Corps of Engineers Mississippi River Commission (1948)

common cone penetrometer for use in soil exploration (Lunne et al. 1997). It is now considered the standard modern field penetrometer, manually operated, providing automatic data acquisition and digital readouts of penetration resistance during use, and producing graphs of resistance as a function of depth.

In the laboratory, controlled-mechanism penetrometers have been developed for more sensitive testing of soils of various consistencies and volumes. Generally deployed on a laterally constrained z-stage to enable only vertical motion and equipped with force sensors capable of digital recording, they have been used to explore the mechanisms of deformation during penetration (Kochan et al. 1989; Cil 2011) and, when upwards vertical motion is prohibited via a lead screw, to examine the relaxation of the soil post penetration (Atkinson et al. 2019).

15.2.3 Measurements and Applications

Depending on the application, the standard measurements for cone penetration testing generally involve the vertical force imparted on the cone (often called the *resistance*)—measured in N or other units of force—and the depth of penetration in m or ft. Readouts show the force encountered at a certain depth, or alternatively the depth a penetrometer reaches under a specific weight (force). Additional complexity can be introduced through measurement of the friction along the penetrometer shaft (which contributes to the overall resistance) or the measurement of pore pressure using a tapered piezocone at the penetrometer tip (Lunne et al. 1997; Varney et al. 2001; Jiang et al. 2006).

The vertical force applied to press a cone to a certain depth in the soil is dependent on the cross-sectional area of the cone itself, so the force is often reported as a dimensionless cone index (CI) (Oravec 2009). CI represents the force per unit base area and generally takes the form (Rohani and Baladi 1981)

$$CI = \frac{4F_z}{\pi B^2}, \tag{15.1}$$

where F_z is the vertical force (in N) and B the cone diameter (in m).

The CI is an index of the resistance or *impedance* of the cone and is a compound parameter that involves components of shear, compressive, and tensile strength of the soil in addition to friction along the metal penetrometer shaft (Mulqueen et al. 1977). However, because it is a compound parameter it cannot be used to discern any individual property, and relatively little is known about how CI is affected by soil mechanical properties. CI does not provide an actual physical measurement of the soil strength, only an index to the penetration resistance (Oravec 2009). Even in homogeneous soils, variability in the soil condition will alter the proportion of shear, compressive, and tensile components determined in the CI (Mulqueen et al. 1977).

Over the years, researchers have discovered a number of correlations between CI and various soil characteristics. Rohani and Baladi (1981) developed relationships between CI and civil engineering properties such as shear strength, friction angle, cohesion, density, and shear modulus. While analytical predictions for the standard Waterways Experiment Station cone penetrometer showed good agreement between CI and these basic engineering properties, the relationships were only valid for homogeneous, frictional soils. Alshibli and Hasan (2009) claim that soil properties such as shear strength, permeability, in-situ stress, and compressibility can all be calculated using CPT data, and Carrier et al. (1991) point to the fact that the shear strength of soil, a key component of the resistance to penetration, governs engineering properties like ultimate bearing capacity, slope stability, and trafficability. In contrast, Wong (1989) showed that it was simple to obtain CI from a soil with known properties but difficult to determine the properties independently from the CI values. Mulqueen et al. (1977) investigated the relationship of CPT resistance to engineering properties such as soil strength and moisture content and found that changes in shear and compressive strengths were not reflected in the resulting CI values of soils with high moisture content: that is, the effect of the moisture content was predominant.

Another common index used in cone penetrometer investigations is the cone index gradient with depth (G), which is the slope of the linear portion of a resistance vs. depth curve. It has been shown to indicate relative soil density and strength over a range of depths, whereas CI indicates soil strength at a specific depth (Oravec 2009). As with CI, generally a higher G value indicates stronger soil.

Interpretation of CPT data still relies largely on empirical correlations developed in laboratories and calibration chambers, where soil properties are carefully controlled (Johnson 2003; Butlanska et al. 2012). When these correlative relationships are applied to soil conditions that differ from those of the testing environment, significant errors have been noted (Johnson 2003). Even with such complications, CPT results are routinely and successfully used in multiple industries to obtain valuable soil information.

An economical procedure, the cone penetrometer test is a common investigative tool in geotechnical engineering. The CPT has been widely used in soil studies related to off-road traffic and cultivation, and its use in offshore geotechnical work is commonplace due to ease of deployment. The cone penetrometer is the reference tool for obtaining geotechnical data in burial engineering (often in conjunction with other continuous geophysical profiling techniques), and for assessing burial conditions along pipeline or telecom cable routes (Puech and Foray 2002). Pore pressure-predicting piezocones have also found uses in estimating the consolidation coefficient of soils (Jiang et al. 2006 and references therein) and in offshore geotechnical site investigations (Lunne et al. 1997; Varney et al. 2001). The CPT is even used as a rapid empirical method in the food industry to determine the consistency of a wide variety of solid, semisolid, and nonfood products (Muthukumarappan and Swamy 2017).

A short comparison of relevant parameters of terrestrial versus lunar (and lunar simulant) cone penetrometer testing is presented in Table 15.1 to orient geotechnical engineers to the similarities and differences between the two.

Table 15.1 Comparison of terrestrial and lunar geotechnical investigation methods

Character	Terrestrial	Lunar (in situ and analog)
Main purpose	Civil engineering projects	Scientific exploration
Soil type	Onshore/offshore clay, silt, sand, or gravel	Lunar regolith, lunar regolith simulants
Soil state	Partly or fully saturated	Dry
Penetrometer type	Standardized (10 cm^2, 60° cone)	Not standardized, mini-CPT often used in lab
Penetration mechanism	Generally truck/rig with hydraulic force	Manual or robotic
Penetration force available	Generally 5–20 kN	Generally 0.1–1 kN
Penetration depth	Generally 5–50 m[a]	Lab: mm In situ: m
Measurement bias	Electrical sensors inside penetrometer	Force gage above penetrometer
Measured parameters	Cone resistance, sleeve friction, pore pressure	Penetration resistance, relaxation
Measurement timing	During penetration, during dissipation (if conducted)	During penetration, during relaxation (if conducted)
Use of measured parameters	Site characterization for foundation design, slope stability, etc. Layering and soil parameters obtained through empirical correlations	Scientific understanding of regolith properties, estimates of bearing capacity

[a] Can be carried out to larger depths in boreholes

15.3 Physical Mechanisms

15.3.1 Introduction

Penetration of a cone into a granular material—while a simple procedure—is a complicated process. The failure of grains around the cone leading to an increase in fine material, the contributions of stress at the cone tip and friction along the sleeve/shaft, the development of soil bodies ahead of the advancing cone tip: all make for a mechanically complex process which has been subjected to considerable theoretical treatment. To this day, however, there is no widely accepted theory of failure mechanics during penetration. Rather, empirical correlations dominate terrestrial use after decades of intense laboratory study in a wide range of natural and synthetic materials. This section provides a brief overview of research into the physical mechanics of penetration and, less closely studied, relaxation behavior.

15.3.2 Penetration

Researchers and engineers analyze cone penetration problems using three main methods: experimental investigations using calibration chambers and controlled environments, theoretical analyses concerning bearing capacity and/or cavity expansion, and numerical methods including finite- and discrete-element modeling (Jiang et al. 2006).

Theoretical treatments of the physical mechanisms of deformation at play during the penetration of a cone penetrometer into a granular material are generally based on continuum mechanics models of behavior and ignore the influence of microstructures (individual grains) (Johnson 2003). Most theories assume that shear strength is typically defined by Mohr–Coulomb

$$\tau_f = c - \sigma \tan\phi, \tag{15.2}$$

where c is apparent cohesion (in Pa), ϕ is the angle of internal friction or shearing resistance (in degrees), and σ is the normal pressure (in Pa), and incorporate some form of the ultimate bearing capacity equation introduced by Meyerhof (1957)

$$q_u = cN_{cq} + \frac{1}{2}\gamma B N_{\gamma q}. \tag{15.3}$$

Here q_u is known as the ultimate bearing capacity or penetration resistance (in N/m^2 or Pa), c is the soil cohesion (in Pa), γ the unit weight of the soil (in N/m^3), B the diameter of the penetrometer base and shaft (in m), and finally N_{cq} and $N_{\gamma q}$ are the dimensionless bearing capacity factors for cohesion surcharge and friction surcharge respectively. Another common theory assumes that penetration occurs through a similar Mohr–Coulomb (elastic–plastic) granular medium that produces a monotonically increasing pressure loading that results in the expansion of a series of spherical cavities around the penetrometer (known as the cavity expansion theory), simulating the geometry of the cone (Vesic 1972; Rohani and Baladi 1981; Johnson 2003). Yu and Mitchell (1998) showed that the cavity expansion approach provides more accurate predictions than bearing capacity theory (Jiang et al. 2006).

While most of the most important recent theoretical treatments of penetration theory have involved the use of finite-element and discrete-element modeling (among others), numerical methods will not be discussed in detail in this chapter due to their complexity. Numerical models are instrumental in increasing our understanding of the physical mechanisms of deformation at the granular level, and the reader is directed to Jiang et al. (2017) and the references therein.

What physically occurs during penetration of a granular material is still an area of active research. Two approaches describe slightly different physical mechanisms, one based on continuum mechanics and the other on the interaction of microstructures at the granular level.

The continuum mechanics approach treats the penetrometer and the granular medium as single, separate bodies. Traditional theory, which predicts a linear increase in stress with depth for homogeneous, unstratified soils, states that during penetration the stresses near the penetrometer tip increase with depth to large peak stresses then decrease upon material failure to constants slightly larger than their initial values. The penetration causes the soil near the penetrometer tip to undergo combinations of compression, shear, and tensile stress in various directions and leads to a complex displacement path, often resulting in high displacement gradients and velocity fields (Jiang et al. 2006). Soil body formation at the leading edge of penetrometer tips (particularly blunt ones) have also been noted as having significant impact on the resistance (Mulqueen et al. 1977).

An approach that predicts nonlinear increases in resistance with depth was introduced by Puech and Foray (2002), refining a model for interpreting shallow penetration cone penetrometer testing in sands. Two phases of penetration were identified: the first phase was characterized by a parabolic increase in resistance associated with the dilational movement of the overburden around the rod, followed by a quasi-stationary linear regime dominated by compression. The first, parabolic phase tends to disappear in loose sands and the change in concavity occurs at the first occurrence of compressional mechanisms at the penetrometer tip.

Similar observations of nonlinearity were reported by Meyerhof (1976) and ElShafie (2012). ElShafie et al. (2012) presented a nonlinear model to describe penetration resistance force results in Martian regolith stimulants, taking the form.

$$F_T = F_c + F_s = q_c A_c + q_s A_s, \tag{15.4}$$

where q_c is the cone resistance and q_s the sleeve/shaft resistance (in Pa), A_c and A_s the cone and sleeve area (in m^2).

When combined with estimates of q_c (Puech and Foray 2002) and q_s (Harr 1977), Atkinson et al. (2019) showed that ElShafie's estimate of F_T can be expressed as a parabolic equation in the form

$$F_T = F(z) = \alpha z + \beta z^2, \tag{15.5}$$

with α (in N/m) a function of the unit weight of the soil, bearing capacity factors, and cross-sectional area of the cone, and β (in N/m^2) a complicated function of α and many soil properties including lateral slip lines, coefficients of lateral pressure and angle of internal friction. This model accurately predicted responses of various regolith simulants in a carefully conducted set of laboratory experiments (Atkinson et al. 2019, 2020). While nonlinearity has been identified as being applicable mainly to shallow penetrations of noncohesive, granular, sand-like materials (including regolith simulants), much remains to be discovered concerning the physical and mathematical descriptions of penetration within a continuum mechanics perspective.

The discrete-element approach suggests that granular materials support penetration forces through the development of microstructure elements that consist of individual grains/particles connected to each other by either cohesive bonds or friction contacts (Johnson 2003). During penetration, a microstuctural element in contact with the penetrometer deforms elastically until a critical deflection is reached and the element fails in a brittle manner. Once failure occurs, the element fragments are compressed around the penetrometer surface forming a compaction zone extending from the cone tip to its base (Fig. 15.3). The microstructural approach attempts to address contradictions in the application of continuum mechanics theory, which predicts that resistance should not vary with cone angle and base area (Johnson 2003).

15.3.3 Relaxation

The relaxation of stresses around a penetrometer tip has been given insufficient treatment in the literature. Few experiments have been performed and very little has been investigated in terms of physical mechanisms specific to penetrometer testing. Stress relaxation phenomena in general have been successfully modeled using rheological models to aid in identifying the elastic and viscous components of deformation (Roylance 2001; Liingaard et al. 2004; Mitchell and Kenichi 2005; Atkinson et al. 2019).

Rheological models are conceptually useful and, while they reflect the real behavior of soils (Liingaard et al. 2004), they assume simple linear relationships in both the elastic and viscous components of deformation in describing the complex relationships in granular materials (Atkinson et al. 2019). The most common application of rheological models to relaxation behavior has been in the description of soil relaxation (Lacerda and Houston 1973; Rao et al. 1975; Kuhn 1987), but it has also found use in food science (Peleg and Normand 1983).

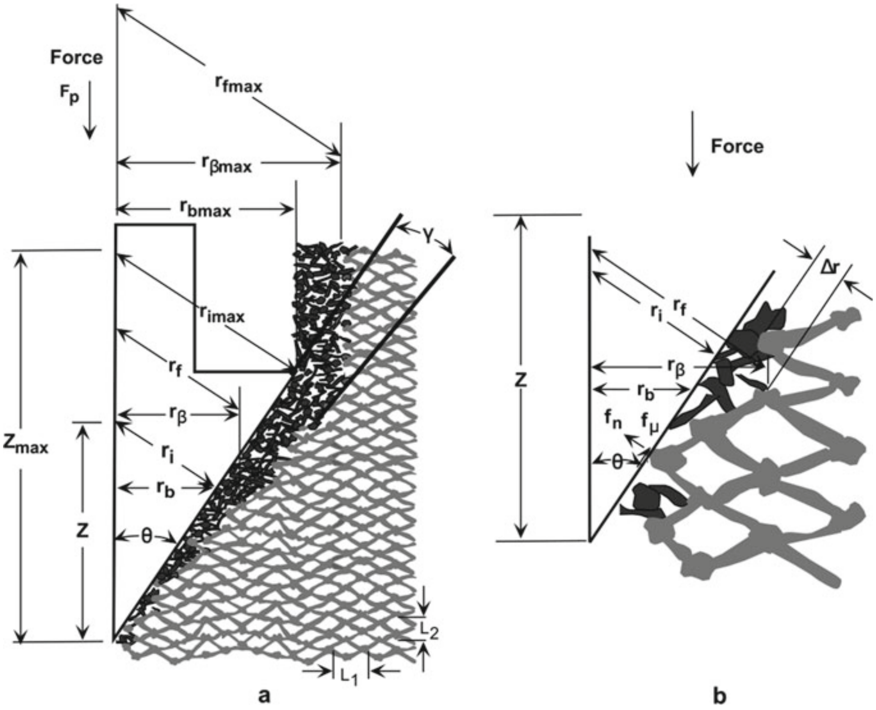

Fig. 15.3 A representation of the process of cone penetrometer moving through a granular material, including the geometric parameters and compaction zone. Note that the various parameters indicated are described in detail in the original publication and not described here. Modified from Johnson (2003)

The most widely accepted form of the rheological model is the "Maxwell" model (Liingaard et al. 2004), consisting of an external Hookean spring connected in parallel to any number of Maxwell arms (themselves consisting of a spring and viscous Newtonian dashpot in series) (Fig. 15.4). The springs represent instantaneous elastic deformation of the body while the dashpots provide a viscous, time-dependent response to deformation (Atkinson et al. 2019). Upon deformation, all the input energy goes into compression of the springs and the dashpots then energy is gradually dissipated resulting in exponential decay (Rao et al. 1975).

A normalized mathematical formula for this relaxation behavior is presented by Peleg and Normand (1983) and modified by Atkinson et al. (2019) as

$$\frac{\sigma(t)}{\sigma_{max}} = \epsilon\left(k_e + \sum_{i=1}^{n} k_i e^{-\frac{t}{\tau_i}}\right), \tag{15.6}$$

which closely resembles the more general formula for universal relaxation provided by Snieder et al. (2017)

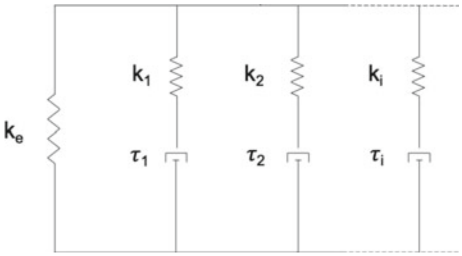

Fig. 15.4 Rheological relaxation model including springs and dashpots representing elastic and viscous behavior (respectively). *Source* Atkinson et al. (2019)

$$\frac{\sigma(t)}{\sigma_{max}} = \epsilon\left(k_e + \int\limits_{\tau_{min}}^{\tau_{max}} \frac{1}{\tau}e^{-\frac{t}{\tau}}d\tau\right). \tag{15.7}$$

In these equations, $\sigma(t)$ is the vertical stress (in Pa) exerted on a probe tip as a function of time (t), σ_{max} the maximum penetration resistance experienced by the probe (in Pa), ϵ the resulting strain in the surrounding material, k_e the residual load supported by the material after relaxation has occurred, k_i and τ_i the elastic and viscous components of the Maxwell arms, and τ_{min} and τ_{max} the limiting relaxation times.

While the physical mechanisms of both penetration and relaxation in cone penetrometer testing are poorly understood, the information gathered during decades of use has yielded extremely useful results for investigating and predicting the behavior of soils. From buried cables, foundations for buildings, landing strips for airplanes through to the regolith on the surface of extraterrestrial bodies, the penetrometer is an excellent tool for characterizing and predicting soil behavior.

15.4 Lunar In-Situ Penetrometer Investigations

Despite repeated missions to Earth's nearest celestial neighbor in the 1960s and 1970s (and, notably, none thereafter), the lunar environment, its soils, and the interplay between the two is not well understood. Direct in-situ measurements of the lunar regolith were made possible by the landings and subsequent exploration of the Luna 9 and 13 rovers in 1966, the Surveyor 7 surface sampler in 1968, two Lunokhod rovers in 1970 and 1973, and the manned Apollo missions from 1969 to 1972. Laboratory measurements of returned surface samples represent a very small fraction of the overall surface material (Oravec 2009).

The Luna 9 spacecraft was the first to survive a lunar landing, giving immediate information about the surface strength, while Luna 13 carried a conical indentor that used the impulse from a small solid-fuel jet engine to press into the lunar regolith (Cherkasov and Shvarev 1973). Initial regolith properties such as bearing capacity were investigated by the Surveyor 7 surface sampler through impact and trenching tests, though as further exploration would show, many of the inferred values of regolith strength determined from these measurements were near the lower bounds (Carrier et al. 1991). The lunar regolith data from Surveyor missions were augmented by the later Apollo missions, whose measured soil property values are expected to be much closer to reality (Oravec 2009).

Autonomous Lunokhod (1 and 2) operations resulted in over 1000 measurements of the physical properties of the lunar regolith and covered over 50 km of terrain, representing the broadest coverage of lunar regolith strength available (Gromov 1998). An original analysis of these data was undertaken by Durgunoglu and Mitchell (1973), and more recent re-analysis by ElShafie and Chevrier (2014) confirmed many of the previous results. The astronauts of the Apollo missions performed extensive soil mechanics experiments that generally increased in complexity with each subsequent landing. From the interaction of the Apollo lunar module with the lunar surface, to famous footprints and specially designed penetrometer tests, the Apollo program provided the most detailed investigation of lunar regolith mechanics to date.

Penetrometer testing constituted a significant part of the overall soil property investigation of the lunar surface by both Soviet and American scientists. Penetrometers deployed autonomously on the Lunokhod rovers or operated manually by Apollo astronauts, along with additional geotechnical testing, provide the best estimates of lunar regolith bearing capacity, density, cohesion, friction angle, and void ratio. A broad overview of the geotechnical results of all lunar missions is presented in Table 15.2.

The most important measurements of the in-situ strength of lunar regolith come from the cone penetrometer tests made on the Lunokhod 1 and 2 robotic roving vehicles and manually operated tests on Apollo missions 14, 15, and 16 (Carrier et al. 1991).

The Lunokhod 1 robotic rover, deployed in 1970 on the Soviet Luna 17 mission, was equipped with a cone-vane penetrometer, a specialized device consisting of a combination conical penetrometer (5-cm^2 base area and 4.4-cm height, with a 60° apex angle) and shear-vane (7 cm in diameter, with four cone vanes at 90°) for measuring both penetration and torque resistance (Fig. 15.5). The device operated when the rover was stationary and deployed vertically into the soil to a maximum depth of 10 cm (and 196 N) and rotated while a set of sensors recorded the penetration depth, resistance force, rotation angle, and rotation force (torque) (Oravec 2009). In total, 327 tests were performed along a 5-km traverse near the Sea of Rains.

Typical Lunokhod 1 results, shown in Fig. 15.6, were analyzed (Mitchell et al. 1972) using the bearing capacity theory specifically developed for evaluating lunar penetrometer data (Durgunoglu and Mitchell 1973). While the surface locations of each penetration were not specifically described, a generalized horizontal section of the lunar surface (including crater slopes, rims, and rocky areas) was inferred, along with evidence that the strength of crater rims was generally higher than that of intercrater locations and that a decrease in the crater diameter resulted in a decrease in the strength of the regolith at the rim (Oravec 2009). The Lunokhod 2 rover traversed through a region of the Lemonnier crater for a distance exceeding 40 km in a transitional zone from the lunar mare (generally basaltic) to the highlands (generally composed of anorthosite), taking many additional penetrometer readings (Leonovich

Table 15.2 An overview of lunar soil/surface properties and the associated missions. Combined and modified from Gertsch et al. (2008) and Heiken et al. (1991). For complete references of the data, please see the original publications

Mission	Basis	Density [g/cm^3]	Cohesion [kPa]	Friction angle [°]
Orbiter	Boulder track analysis		0.35	33
Surveyor 1	TV and landing data		0.15–15	55
Surveyor 1	TV and landing data	1.5	0.13–0.4	30–40
Luna 13		0.8		
Surveyor 3	Soil mechanics surface sampler, TV and landing data			>35
Surveyor 6	Vernier engine		>0.07	35
Surveyor 6	Attitude jets		0.5–1.7	
Surveyor 3,7	Soil mechanics surface sampler		0.35–0.7	35–37
Lunar Orbiter	Boulder track analysis		0.1	10–30
Lunar Orbiter	Boulder track analysis	0.5	21–55	
Apollo 11	Footprints, lunar module landing data, crater slope stability		Consistent with Surveyor model	
Apollo 11	Penetration tests in LRL bulk soil sample		0.3–1.4	35–45
Apollo 11	Penetration of core tubes, flagpole, SWC shaft		0.8–2.1	37–45
Apollo 11		1.54–1.75		
Apollo 11		0.74–1.75		
Apollo 11		1.81–1.92		
Apollo 11		1.6–2.0		
Apollo 12	Footprints, lunar module landing data, crater slope stability		Consistent with Surveyor Model	

(continued)

Table 15.2 (continued)

Mission	Basis	Density [g/cm^3]	Cohesion [kPa]	Friction angle [°]
Apollo 12	Penetration of core tubes, flagpole, SWC shaft		0.6–0.8	38–44
Apollo 12	Cone penetrometer		0.17–2.7	25–45
Apollo 12		1.80–1.84		
Apollo 12		1.55–1.90		
Apollo 12		1.7–1.9		
Luna 16		1.2		
Lunokhod 1		1.5–1.7		
Apollo 14	Soil mechanics trench		<0.03–0.3	35–45
Apollo 14	Apollo simple penetrometer		≥ Surveyor model	
Apollo 14	MET tracks			37–47
Apollo 14		1.45–1.6		
Apollo 15		1.35–2.15		
Apollo 15	Measured at Station 8	1.92–2.01		47.5–51.5
Apollo 11, 12, 14, 15		1.76	0.55	43
Apollo 15	SRP data and soil mechanics trench		1.0	50
Apollo 16	SRP Station 4		0.6	46.5
Apollo 16	SRP Station 10		0.37	49.5
Apollo 16	SRP Station 10		0.25–0.6	47–50
Apollo 16	Drill core open hole		1.3	46.5
Apollo 17	Drill core open hole		1.1–1.8	30–50
Apollo 17	LRV		0.17	35
Apollo 17	North, East, and South Massifs		1	26–50

et al. 1971, 1976). The results of the Lunokhod measurements indicated a bearing capacity ranging from 0.2 to 1.0 kN/m^2, with a most probable of 0.34 kN/m^2, and a range of shear strengths from 0.03 to 0.09 kN/m^2, with a most probable value of ~0.048 kN/m^2 (Cherkasov and Shvarev 1973; Zacny et al. 2010).

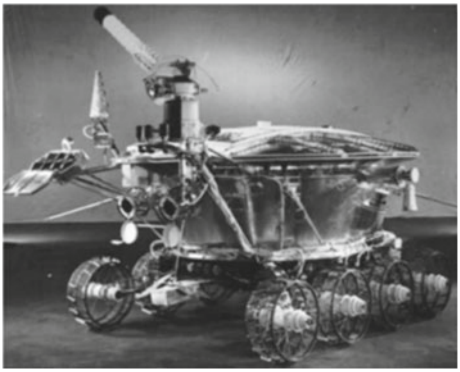

Fig. 15.5 The Soviet Lunokhod 1 robotic roving vehicle. The rover landed in Mare Imbrium in 1970. *Source* Carrier et al. (1991)

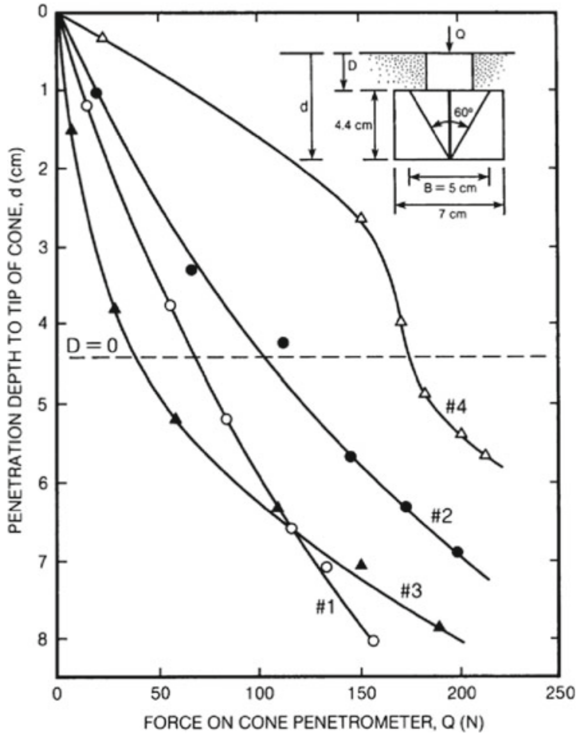

Fig. 15.6 Typical cone penetrometer resistance data, obtained by the Lunokhod 1 automated rover, for the lunar surface material in different areas of its landing site. *Source* Carrier et al. (1991)

The manned Apollo missions, beginning with Apollo 11 in 1969, ushered in a three-year period of intense study of the lunar surface including the properties of the regolith. Apollo 11 and 12, the first two American lunar missions, carried no specific lunar soil testing devices. Estimates of shear strength were limited to interactions with the lunar surface including the landing of the Lunar module, astronauts walking on the surface (the famous footprint), penetration into the soil by coring tubes, an equally famous flag pole, and the solar wind composition shaft (Carrier et al. 1991). These various interactions suggested that the surface was at least as strong as predicted by the Surveyor estimates (Costes et al. 1969).

Apollo 14, landing in early 1971, deployed what became known as the Apollo Simple Penetrometer (ASP): a 0.95-cm diameter, 68-cm long, 30° cone penetrometer used to determine the difference in penetration resistance at various locations along the lunar surface (Carrier et al. 1991). Measuring resistance using the ASP was performed in a rather circumspect manner: Astronaut Mitchell (having had his one- and two-handed pressing force measured prior to the mission) operated the ASP by pressing it as far as he could into the surface using one hand, marking the depth of penetration, then using both hands to penetrate to a maximum depth thereby generating a rough resistance force vs. depth curve. These estimates of force were related to values of cohesion and internal friction angle, which were later compared to Surveyor data and found to be somewhat higher.

The Apollo 15 and 16 missions in 1971 and 1972 made use of an advanced cone penetrometer for measuring lunar regolith properties, known as the Self-recording Penetrometer (SRP) (Fig. 15.7), developed in the Geotechnical Research Lab at the Marshall Space Flight Center Space Science Lab. Designed with a detachable penetrometer portion, a rotating drum recording unit, and various probe components, the instrument provided a constant force-versus-depth profile. As the probe was pushed into the surface with a downward force, a gold-plated cylindrical drum rotated corresponding to the applied force and was simultaneously scratched by a stylus according to the depth of penetration (Carrier et al. 1991). The drum was scribed in situ and returned to Earth for analysis. The SRP included three interchangeable 30° cones of base areas 129, 133, and 645 mm^2, capable of a maximum load of 111 N and depth of 75 cm (Johnson et al. 1995).

Six cone penetometer tests were performed during Apollo 15, all near the lunar module and all performed by Astronaut James Irwin. Costes et al. (1969) reported that two SRP measurements were made within and adjacent to a lunar roving vehicle track, and two others made adjacent to and at the bottom of a 30-cm deep trench with

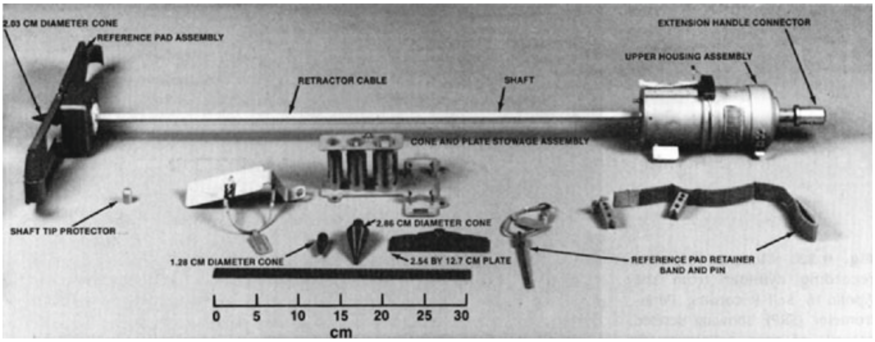

Fig. 15.7 Photo and explanatory diagram of the Self-Recording Penetrometer (SRP) used on the Apollo 15 and 16 missions. *Source* Carrier et al. (1991)

a vertical sidewall. During Apollo 16, ten measurements using the SRP were made by Astronaut Charlie Duke at Bench Crater and the ALSEP site.

The resulting soil mechanics data, in the form of handwritten plots of the penetrometer resistance stress as a function of the depth of penetration, mainly provide a lower bound to the soil strength as slippage of the surface reference pad made it difficult to accurately determine the depth of penetration (Oravec 2009). Estimates of cohesion and the internal friction angle of lunar regolith from the SRP are 0.25–1.0 Pa and 46.5–51.5°, respectively (Carrier et al. 1991).

Oravec (2009) used CI measurements from Apollo 15 and 16 SRP data to determine the cone index gradient G as a function of depth. G ranges from <3 to >9 kPa/mm were calculated, with little apparent correlation with depth (though it is noted that high G values may correspond to encountering rocks in the subsurface), as shown in Table 15.3.

Integrating all the data available, Carrier et al. (1991) derived and recommended "typical" intercrater values of cohesion and friction angle to use when modeling the behavior of the lunar surface (Table 15.4).

Table 15.3 Lunar cone index gradient terrain estimates near Apollo 15 and 16 landing sites. Modified from Oravec et al. (2010), reproduced by permission of Heather Oravec

Mission	Location	Estimated depth [cm]	Cone index gradient, G [kPa/mm]
Apollo 15	Adjacent to trench	8.25	4.06
Apollo 15	In rover track	5.25	4.36–7.59
Apollo 15	Adjacent to rover track	<11.25	>2.98
Apollo 16	Uphill, top of crater	20	3.37–3.86
Apollo 16	Near rover track	8[a]	6.30–9.85

[a] Penetrometer may have hit rock

Table 15.4 Recommended typical values of lunar soil cohesion and friction angle (intercrater areas). Modified from Carrier et al. (1991), reproduced by permission of the Lunar and Planetary Institute, Houston

Depth range [cm]	Cohesion, c [kPa]		Friction Angle, φ [°]	
	Average	Range	Average	Range
0–15	0.52	0.44–0.62	42	41–43
0–30	0.90	0.74–1.1	46	44–47
30–60	3.0	2.4–3.8	54	52–55
0–60	1.6	1.3–1.9	49	48–51

15.5 Lunar Simulants

15.5.1 History

In addition to providing us with important data about the properties of the lunar surface and near-subsurface through the investigations described in Sect. 15.4, the 12 Apollo astronauts also returned 382 kg of lunar material for study here on Earth between 1969 and 1972. To date, an estimated 350 kg of this original material remains for study (Sibille et al. 2006).

The success of future lunar operations (as well as those on other bodies) depends critically on the ability to predict and simulate lunar regolith behavior accurately. Tasks such as construction of lunar habitats, operating surface vehicles, lunar mining, and mitigating the hazard of excessive lunar dust all rely on a fundamental knowledge of regolith behavior. Due to the limited supply of real lunar material and the need to preserve it, the scientific community has turned to the manufacture of suitable regolith simulants intended to represent specific properties of the lunar surface.

A simulant is a material manufactured from natural or synthetic terrestrial components (including meteors) for simulating one or more physical and/or chemical properties of the lunar soil (Sibille et al. 2006). Due to the rather limited variation in regolith composition on the lunar surface, most terrestrial stimulants contain some basaltic or sandy-silicate materials, often ground to a grain-size distribution resembling that of the returned lunar material. The manufacturing of terrestrial simulants generally requires knowledge of the special properties needed for the intended exploration disciplines. For example, terrestrial simulants needed for resource-focused extraction disciplines require chemical and mineralogical similarity to the lunar regolith, while geotechnical researchers require large volumes of simulants with similar mechanical/physical behavior.

Simulants can only approximate the behavior of lunar soil. The unique lunar environment creates regolith properties that are not found in terrestrial soils. Lunar regolith is expected to be dramatically frictional and dilatant compared to terrestrial analogs, particularly at low confining pressures (caused by the absence of a significant lunar atmosphere), which can lead to nonlinear behavior and will strongly affect the behavior of engineered lunar structures such as foundations (Klosky et al. 2000). Lunar regolith also contains agglutinates, glass spheres, nanophase iron, and micrometeoroid impact craters on grain surfaces not found in terrestrial soils (Carrier et al. 1991). The extreme angularity, abrasiveness, and invasiveness of lunar regolith and its associated dust has been remarked upon by many, including the Apollo astronauts subjected to its extraordinary behavior on the lunar surface.

Simulants were also critical in predicting the behavior of lunar regolith *before* humans ever landed on the surface. Despite limited knowledge of the lunar surface prior to the first landings, a highly successful set of standard simulants were developed during the Apollo program to test surface systems in preparation for the lunar landings (Sibille et al. 2006). These simulants, known as Lunar Surface Simulants (LSS) 1–5, were used in the development of drills, tools, and lunar roving vehicle

Table 15.5 Soil properties and parameters for single-wheel tests in lunar simulants LSS1–3. Modified from Green and Melzer (1971)

Soil Parameter	Method	Average
Penetration resistance gradient [g/cm^3]	–	87.7
Dry density [g/cm^3]	Gradient *G*	1.59
	Gravimetric	1.67
Moisture content [%]	–	0.9
Relative density [%]	Gradient *G*	42
	Gravimetric	54
Average friction angle [°]	Triaxial (secant)	39
	In-situ plate	35
	Sheargraph	29
	Bevameter	22
Average cohesion [kPa]	Trenching tests	0.45
	Bevameter	1.01
	Sheargraph	2.07

maneuvers/systems using crushed basalts from Napa, CA, USA (Sibille et al. 2006; Oravec 2009). Classified as “granular with angular to sub-angular grains” (Green and Melzer 1971), these materials no longer exist and the library of documents describing their compositions and properties is incomplete (Sibille et al. 2006). The most comprehensive overview of LSS properties is provided in Oravec (2009), and Table 15.5 presents some general parameters derived from trafficability tests.

Since the creation of the LSS materials, additional simulants have been developed to serve a variety of purposes and investigations throughout the past several decades. Three of these—JSC-1A and its predecessor JSC-1, the NU-LHT series, and the GRC series (GRC 1 and 3)—will be introduced and briefly described. While other simulants have been created for specific purposes, these three simulant families are of interest for two reasons: (1) they represent lunar mare, lunar highland, and specifically geotechnical simulants, and (2) they have all been used in both manual and controlled-mechanism penetrometer investigations for the purposes of predicting lunar surface behavior. The Planetary Simulant Database at the Colorado School of Mines (https://simulantdb.com/) contains a complete listing of current lunar simulants.

15.5.2 JSC-1 and JSC-1A

15.5.2.1 JSC-1

The JSC series of lunar simulants is one of the best known and widely used simulant families ever produced, beginning in the 1990s with the JSC-1 lunar all-purpose simulant generated at the Johnson Space Center (JSC) for the purposes of developing lunar EVA suits (Sibille et al. 2006).

JSC-1 is a general-use mare simulant with low titanium content made from volcanic ash in the San Francisco lava field near Flagstaff, AZ, on the flank of the Mirriam cinder cone (Sibille et al. 2006). It is a glass-rich crushed basaltic ash containing rich oxidized forms of silicon, aluminum, iron, calcium, and magnesium that approximates the bulk chemical composition and mineralogy of the Apollo 14 sample 14163 (McKay et al. 1993; Klosky et al. 2000). Its mineralogy includes olivine, pyroxene, ilmenite, plagioclase, and basaltic glass (Sibille et al. 2006), and it is considered a well-graded silty sand (Klosky et al. 2000).

The most thorough geotechnical analysis of JSC-1 was performed by Klosky et al. (2000), though they note that previous authors (McKay et al. 1993; Willman et al. 1995; Perkins and Madson 1996) had already investigated the simulant's specific gravity, grain-size distribution, and mineral content. Using vibratory compaction to simulate the assumed depositional characteristics of real lunar soil, they performed triaxial compression and isotropic vacuum unloading experiments to determine JSC-1's shear and elastic properties: deviatoric stress and axial strain to axial stress, friction angle, cohesion, Young's modulus, and bulk modulus. They describe high values of cohesion (from ~4 kPa to over 14 kPa) and friction angle (44.4–53.6°) that increase with relative density with maximum and minimum densities of 1.83 and 1.43 g/cm^3 respectively. Perkins (1991) reported friction angles between 41 and 60° and cohesion values between 0.1 and 2.5 kPa.

While ~12,000 kg of JSC-1 was produced, it was widely distributed to researchers and not tracked, stored, or utilized properly. As a result, little is known about how much is left, and what condition it is in (Sibille et al. 2006).

15.5.2.2 JSC-1A

After the original volume of the JSC-1 simulant was exhausted, NASA commissioned the production of another 16 tons (~14,500 kg) of a similar simulant through a coordinated grant in 2005. This included 14 tons of a JSC-1 clone called JSC-1A and one ton each of a coarse (JSC-1AC) and fine (JSC-1AF) version, all produced at the same quarry as the original (Zeng et al. 2010a). JSC-1A is no longer commercially obtainable, but costs ~$20,000 per ton when available.

As with JSC-1, JSC-1A approximates a low-titanium mare regolith and contains major crystalline phases of plagioclase, pyroxene, olivine, and minor oxide phases of ilmenite and chromite (Alshibli and Hasan 2009), though the presence of plagioclase is disputed by Ray et al. (2010).

The chemical/mineralogical composition of JSC-1A, along with its physical and strength properties, engineering properties, and geotechnical properties have all been investigated and characterized by various authors. Ray et al. (2010) characterized JSC-1A by X-ray diffraction (XRD), scanning electron microscope (SEM), differential thermal and thermo-gravimetric analyses, chemical analysis, and Mössbauer

Table 15.6 Chemical compositions of the JSC series of lunar simulants compared to a lunar sample from Apollo 17. Modified from Ray et al. (2010)

Constituent oxides	JSC-1 [%]	JSC-1A [%]	Apollo 17 Sample 70051 [%]
SiO_2	47.2	45.7	42.2
Al_2O_3	15.0	16.2	15.7
CaO	10.4	10.0	11.5
MgO	9.0	8.7	10.3
FeO	7.4	–	12.4
Fe_2O_3	3.4	12.4	–
Na_2O	2.7	3.2	0.2
K_2O	–	0.8	0.1
TiO_2	1.6	1.9	5.1
P_2O_5	–	0.7	–
MnO	–	0.2	0.2

spectroscopy. The results, showing the weight percentage (wt%) composition of JSC-1A as compared to JSC-1 and samples from Apollo 17, are presented in Table 15.6. The high glass content—similar to the lunar soil—also allowed for the creation of various glass preforms such as glass hairs and beads (Fig. 15.8).

The physical and strength properties of JSC-1A were investigated by Alshibli and Hasan (2009), who compared its particle-size distribution to that of the range of returned Apollo samples and found it to be within ±1 standard deviation (SD). The specific gravity of the simulant was found to be 2.92 compared to 2.90 for JSC-1 (McKay et al. 1993) and 2.9–3.4 for Apollo samples (Carrier et al. 1991), with a maximum and minimum density of 2.106 and 1.556 g/cm^3 respectively, compared to reported values of 1.93 and 0.87 g/cm^3 (Carrier et al. 1991). Triaxial tests provided average ranges for the Young's modulus, shear modulus, and Poisson's ratio (Alshibli and Hasan 2009), while scanning electron microscope (SEM) images showed highly

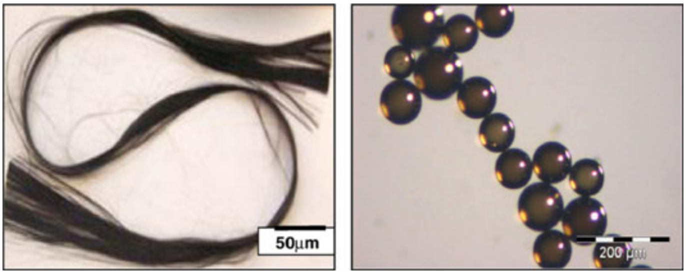

Fig. 15.8 Left: Glass fibers prepared from JSC-1. Right: Hollow glass microspheres produced from JSC-1. Modified from Ray et al. (2010)

angular shapes and surface crevices reminiscent of lunar regolith images. Finally, a peak friction angle range of ~40–59°, increasing with density, was measured.

A geotechnical analysis of the simulant was performed by Zeng et al. (2010a). In addition to defining particle-size distributions, specific gravity, and maximum/minimum densities similar (though not identical) to Alshibli and Hasan (2009), triaxial testing determined the stress/strain characteristics as well as the shear behavior under increasing normal stress. Cohesion was found to be too low to measure, and the peak friction angle was found to be high and to increase with density. The low cohesion value described by Zeng et al. (2010a) was eventually determined to be exceptionally small, from 0 to 1.1 kPa by Li et al. (2013).

15.5.2.3 NU-LHT

The first general lunar highlands regolith simulant was developed in the early 2000s by the USGS and named the NU-LHT series. NU-LHT-1M was a pilot simulant, and −2M a prototype, matching the modal mineral and glass content, average chemical composition, and grain-size distribution of Apollo 16 regolith samples as closely as possible (Stoeser et al. 2010). It is not known if NU-LHT simulant is currently available, but it had a cost similar to JSC-1A at ~$20,000 per ton.

The composition of NU-LHT is a combination of mostly intrusive igneous rocks: Stillwater norite, anorthosite, hatzburgite, and Twin Sisters dunite. The simulant included pseudo-agglutinates formed of partially melted Stillwater mill waste (from the Stillwater Mining Company of Nye, MT), while fully melted waste constituted what was termed “good glass” (Stoeser et al. 2010). NU-LHT-1M consisted of 80% crystalline, 16% agglutinate, and 4% glass components, while −2M consisted of 65, 30, and 5% respective components. The bulk chemistry is reported in Table 15.7.

Geotechnical properties of NU-LHT-2M were investigated by Zeng et al. (2010b), including the particle-size distribution, specific gravity, maximum and minimum densities, triaxial testing, and peak friction angles. The particle-size distribution of NU-LHT-2 M falls within ±1 SD of the lunar soil reported by Carrier et al. (1991), except at the finest particle sizes. It is classed as a well-graded silty sand, and a specific gravity of 2.749 was identified as being lower than that of typical lunar regolith. The maximum dry density was 2.057 g/cm^3 and the minimum 1.367 g/cm^3

Table 15.7 Composition of NU-LHT-1M prototype. From The Planetary Simulant Database (https://simulantdb.com/), reproduced by permission of the USGS

Constituent oxides	Wt %
SiO_2	47.6
Al_2O_3	24.4
FeO	4.3
MgO	8.5
CaO	13.1
Na_2O	1.4

(compared to 1.93 and 0.87 g/cm^3 respectively for lunar soils). A peak friction angle of 36–40.7° was determined to be lower than typical lunar soils, but that it increased with density.

15.5.2.4 GRC-1 and GRC-3

The GRC-1 and GRC-3 lunar simulants were developed at Glenn Research Center around 2009–2011 as purely geotechnical simulants designed for testing roving vehicle wheel traction in lunar soils (GRC-1, Oravec 2009) and excavation studies (GRC-3, He et al. 2011). They were developed as a readily available sand mixture and, at an affordable cost of $250 per ton (compared to ~$20,000 per ton for JSC-1A or NU-LHT) (He et al. 2011), facilitated the use of large quantities for vehicle mobility and excavation testing. Composed primarily of quartz sand, the GRC series is a combination of commercially available sands from the Best Sand Corporation of Chardon, Ohio and, in the case of GRC-3, a natural loess (Bonnie silt) from Burlington, Colorado comprises a finer component. GRC-1 is currently available from Black Lab (Covia) in Chardon, Ohio; it is not known if GRC-3 is commercially available at this time.

Geotechnical properties of GRC-3 were investigated by He et al. (2011), with the standard determination of particle-size distribution, specific gravity, maximum and minimum densities, peak friction angle, cohesion, shear and stress–strain behavior. The particle-size distribution slightly exceeds the ±1 SD limit of typical lunar soils at both median and very fine particle sizes and it is classified as a silty sand. The specific gravity, 2.633, is lower than that of lunar soils, while the maximum and minimum densities (1.939 and 1.520 g/cm^3) are within the typical lunar soil range. The peak friction angle of 37.8–47.8°, as with both JSC-1A and NU-LHT-2M, is lower than that of typical lunar soils but increases with density. Cohesion was determined to be essentially negligible (as expected for sands).

A summary of the pertinent geotechnical, physical, and strength properties of the simulants JSC-1, JSC-1A, NU-LHT-2M, and GRC-1 and -3 are shown in Table 15.8, and compared to the values of typical lunar soils as determined by Carrier et al. (1991).

Table 15.8 Summary of pertinent simulant properties compared to recommended values representing lunar regolith

Property	Lunar Soil[a]	JSC-1	JSC-1A	NU-LHT	GRC-1	GRC-3
Specific gravity	2.9–3.4	2.90	2.92	2.75	2.58	2.63
Max density [g/cm^3]	1.93	1.83	2.11	2.06	1.89	1.94
Min density [g/cm^3]	0.87	1.43	1.56	1.37	1.60	1.89
Peak friction angle [°]	41–55	41–60	40–59	36–41	~ 39	38–48
Cohesion [kPa]	0.4–3.8	0.1–2.5	0.0–1.1	–	–	–

[a] All depth ranges

15.6 Penetrometer Tests in Lunar Simulants

15.6.1 Introduction

The return of over 300 kg of lunar rocks and soil from the Apollo missions of the 1960 and 1970s enabled detailed investigations—including penetrometer testing—of the regolith's mechanical properties. The first lab measurements of the lunar regolith's shear strength were performed in 1969 in the Lunar Receiving Lab at the NASA Manned Spacecraft Center (now known as the JSC) and were the first of many performed on the samples returned by Apollo 11.

Shear investigations consisted of a standard penetrometer test where a flat hand penetrometer was pressed into several hundred grams of compacted lunar regolith (Carrier et al. 1991) then sieved to remove larger clasts (>1 mm) and kept in a dry nitrogen atmosphere to prevent adsorption of ambient moisture. The results show generally increasing penetration force as a function of depth, with higher-density samples more resistant to penetration at all depths (Table 15.9). Similar penetration tests were performed by Jaffe (1971) on 6.5 g of returned Surveyor 3 regolith.

While no additional laboratory penetrometer tests were apparently performed on the returned lunar soil, it is worth mentioning relevant shear investigations that complement the CPTs. Carrier et al. (1972, 1973) performed three direct shear tests

Table 15.9 Laboratory hand penetrometer measurements on lunar soil samples from Apollo 11 sample no. 10084. Modified from Carrier et al. (1991), reproduced by permission of The Lunar and Planetary Institute, Houston

Test	Density [g/cm^3]	Force [N]	Area [cm^3]	Pressure [kPa]	Penetration [cm]
1	1.36	<1.8[a]	0.316	<57	0.64
2	1.36	<1.8[a]	0.316	<57	1.96
3	1.36	<1.8[a]	0.316	<57	1.96
4	1.36	<1.8[a]	0.316	<57	1.96
5	1.36	3.1	2.68	11.4	2.01
6	1.77	1.8	0.316	57	0.81
7	1.77	5.1	0.316	171	1.70
8	1.77	<1.8[a]	0.316	<57	0.64
9	1.77	9.8	0.316	308	2.54
10	1.77	5.8	0.316	183	2.11
11	1.77	38.7	2.68	143	1.70
12a	1.80	28.9	2.68	108	0.66[b]
12b	1.80	79.8	2.68	297	1.96[b]

[a] Penetrometer did not meet with sufficient resistance, tabulated force is weight of penetrometer

[b] Penetrometer was removed after achieving 108 kPa at 0.66-cm depth, then reapplied at the same place until achieving 297 kPa at 1.96-cm depth from original sample surface

(in a vacuum) on 200 g of Apollo 12 soil. They noted that the resulting measured cohesion and friction angle were significantly lower than those of a basaltic simulant, which they attributed to the crushing of weak particles such as agglutinates and breccias unique to the lunar regolith. More precise shear tests (triaxial, direct shear, etc.) were performed on Surveyor 3 scoop samples (Scott 1987) and Luna 16 and 20 samples (Leonovich et al. 1974, 1975).

15.6.2 Apollo Era

The early 1970s saw the first recorded penetrometer experiments on the newly created lunar soil simulant (LSS) (see Sect. 15.5). Costes et al. (1971) performed CPTs in LSS and Yumi sand of various grain-size distributions and consistencies under terrestrial conditions and on-board parabolic flights achieving 1/6, 1, and 2 g in order to investigate the effect of gravity. The results indicated that the average penetration resistance (q_c) and the average rate of change in q_c with depth (z) of the simulants decrease monotonically with decreasing gravity (g) and are sensitive indicators of soil bulk dry density, void ratio, and relative density (Fig. 15.9). They further claimed that q_c and G could be used with bearing capacity theory to determine in-situ shear strength and developed these analytical methods for application to crude soil penetration data from Apollo 11 and 12, determining preliminary measures of cohesion and other soil properties.

An extensive experimental program was undertaken in 1971 to determine the penetration resistance of an unnamed lunar soil simulant and translate the detailed relationships to the lunar surface (Houston and Namiq 1971). The simulant was

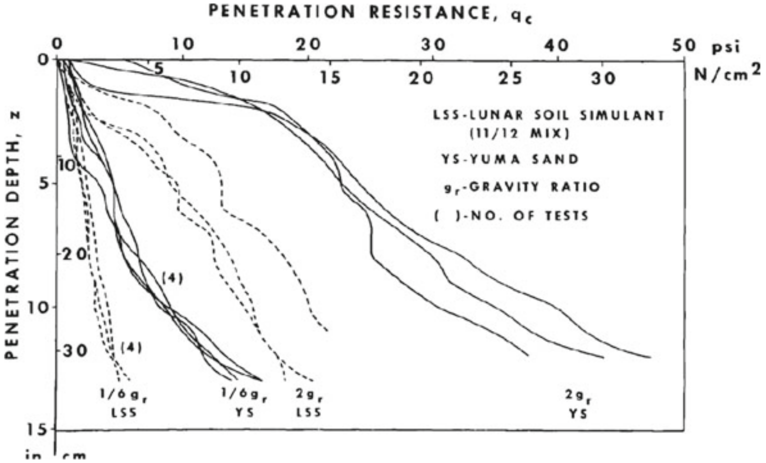

Fig. 15.9 Cone penetration resistance (q_c) versus penetration from tests on Yuma sand and a mix of LSS 11/12 performed under varying gravity conditions. Modified from Costes et al. (1971)

prepared by mixing crushed basalt powder with basalt sand, selected and modified based on Surveyor and Apollo 11 compositions, gradation curves, and cohesion values. Of particular note was that the authors found the addition of 2% water to the simulant generated enough cohesion to mimic that estimated for lunar regolith cohesion values. This mass percent of moisture is still in use today.

Ultimately, the experimental campaign generated an estimate of ultimate bearing capacity that could be applied to in-situ lunar soils (Houston and Namiq 1971)

$$q_{ult} = \frac{B\gamma}{2} N_\gamma s_\gamma + cN_c s_c + q^{'} N_q s_q, \tag{15.8}$$

where q_{ult} is the unit ultimate bearing capacity (in N/m^2), q' the surcharge stress (in Pa), N_γ, N_c, N_q the dimensionless bearing capacity factors for friction, cohesion, and the surcharge respectively, and finally s_γ, s_c, s_q dimensionless shape factors. The analysis generated an estimate of the variation in G with average void ratio (Fig. 15.10).

Houston and Namiq (1971) concluded that the bearing capacity equation provided a reasonable estimate of G if local shear strength parameters were used (assuming these could be obtained) and predicted that the factor by which the penetration resistance is reduced in lunar gravity (~1/4) is less than the reduction in gravity (1/6). Finally, they predicted that stress penetration gradients could be used to indicate heterogeneity in lunar soil.

A final set of penetration experiments in LSS2 was performed by Durgunoglu and Mitchell (1973), where the application of the authors' analytical models to static CPT measurements showed good agreement (Fig. 15.11). Using a 15° conical penetrometer 2 cm in diameter, manual insertion into simulant prepared over a wide variety of densities resulted in penetration profiles that were compared with

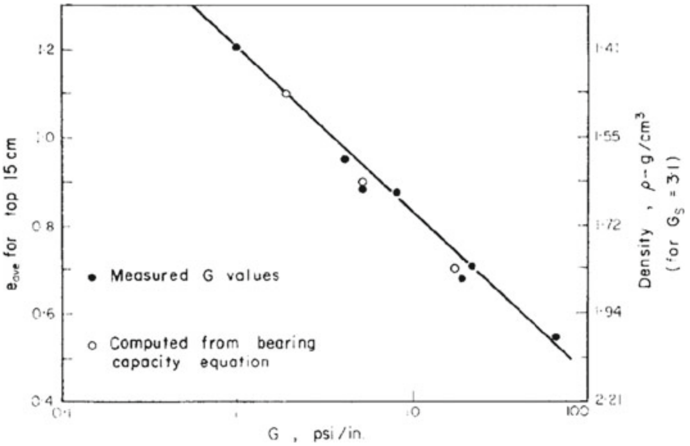

Fig. 15.10 Comparison of measured and computed G values for an unnamed lunar soil simulant under full gravity. *Source* Houston and Namiq (1971)

analytically-predicted penetration resistance using the formula

$$q_f = cN_c s_c + \gamma B N_{\gamma q} s_{\gamma q} \tag{15.9}$$

While not apparent from the figure, low-density (high void ratio, i.e., Test A-1 in Fig. 15.11) predictions were less accurate. The authors explained this decreased model accuracy at lower densities as due to the significant influence of soil compressibility on resistance.

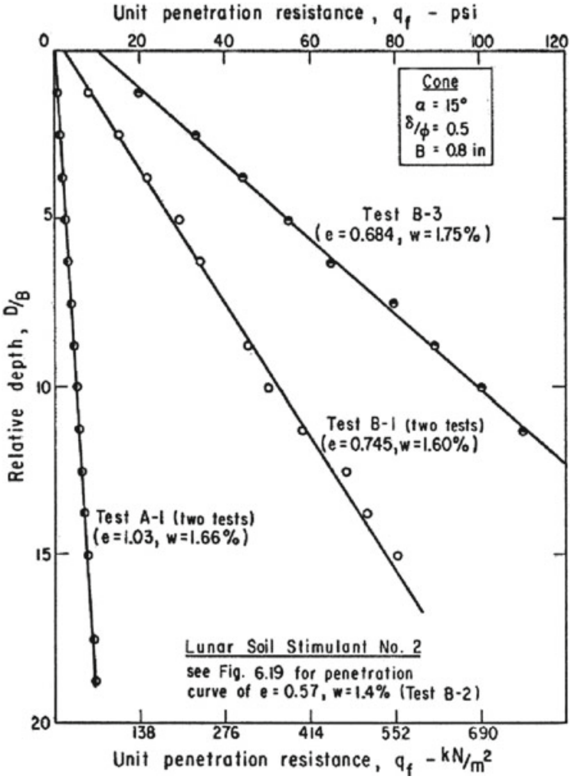

Fig. 15.11 Measured penetration curves for LSS2. *Source* Durgunoglu and Mitchell (1973)

15.6.3 Manual

There was a general hiatus in penetration testing in lunar regolith simulants for roughly three decades until the early 2000s, when a new geotechnical simulant (GRC-1) was being developed at Case Western Reserve University—under a cooperative agreement with the NASA Glenn Research Center—by H. Oravec during her doctoral thesis, in which she used CPT measurements of various permutations to compare the new simulant to lunar trafficability estimates (Oravec 2009).

The penetration experiments were performed by manual insertion (Fig. 15.12) of a 30° field cone penetrometer of two interchangeable cone areas—130 and 323 mm^2—into several different-sized bins (from 55 to 75 cm in diameter) filled in uniform layers using a hopper and compacted to specified densities. The cone-to-container radius ratio $\left(CCR = \frac{r_{container}}{r_{cone}}\right)$ for these experiments ranges from 36 to 43, indicating that dominant edge effects would not be expected. CCR relates the radius of the penetrometer to the radius of the sample container and should generally be greater than 10 to avoid edge effects in confined sample testing.

Four tests of 16 insertions each (at an attempted rate of ~2 cm/s) were analyzed to determine the effect of cone size and repeatability of testing in ambient conditions. For each cone size and depth, the cone index gradient (G) was determined and a generally expected increase in gradient with depth observed (Table 15.10). Oravec (2009) states that the increase is likely due to compaction and compression ahead of the probe.

The determination of G, however, involves an assumption of linearity in the penetration profiles, and nonlinearity can cause a significant difference in the resulting gradient values. Repeated mentions of nonlinear behavior are noted in the study and are most clearly seen in the penetration profiles of higher-density samples for both cone sizes (Fig. 15.13), while low-density samples show more linear behavior. Irrespective of linearity, the mean G showed the expected increase with density (Fig. 15.14).

Fig. 15.12 Cone penetration tests in GRC-1 at the NASA Glenn soils lab. *Source* Oravec (2009), credited to NASA GRC

Table 15.10 Cone index gradient (*G*) in GRC-1 as a function of depth intervals. Modified from Oravec (2009), reproduced by permission of Heather Oravec

Soil depth [mm]	Cone index gradient (*G*) [kPa/mm]
5–15	4.03
15–25	4.01
25–35	4.56
35–45	4.09
45–55	5.06
55–65	4.93
65–75	5.08
75–85	5.79
85–95	5.78
95–105	5.74
105–115	6.91

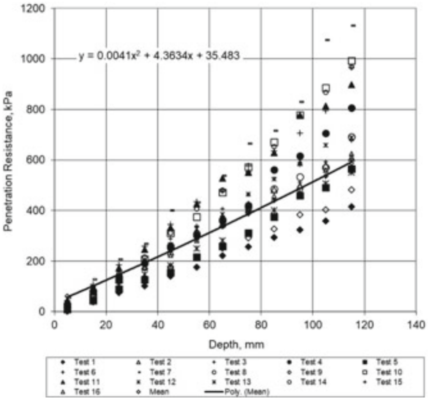

Fig. 15.13 Penetration profiles of the small (left) and large (right) cone penetrometer tests in GRC-1, showing nonlinearity. Modified from Oravec (2009)

After determining the effect of density on *G* at ambient conditions for the GRC-1 simulant, SRP data from Apollo 15 and 16 were analyzed in the same manner. A large range in *G* was predicted, potentially demonstrating regional variation in lunar soil conditions. The lower end of the predicted values (2.22–5.08) for the Apollo 15 tests (Tests 1–4) correspond generally well to those estimated by Mitchell et al. (1972) of 2.98–5.97 (as cited by Costes et al. 1972). Differences between the *G* values for GRC-1 and the lunar estimates are claimed to be due to the ambient testing conditions (pressure and temperature), the presence of moisture in terrestrial samples, boundary conditions of the plastic testing bins, and the artificial sample preparation method using vibration.

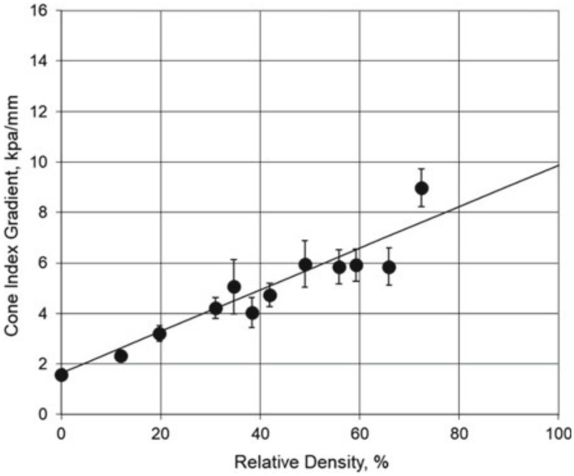

Fig. 15.14 The expected linear increase in cone index gradient *G* as a function of relative density in GRC-1 (with standard deviation). *Source* Oravec (2009)

The response of manual penetration resistance to ice content in icy regolith simulants has been investigated by Mantovani et al. (2016) and Pitcher et al. (2016), using considerably different approaches and control of ambient conditions.

Mantovani et al. (2016) built upon previous work by Honeybee Robotics showing that a percussive cone penetrometer was capable of penetrating lunar regolith with a fraction of the force required using an ordinary field penetrometer. Using a percussive cone penetrometer developed by Honeybee Robotics (Fig. 15.15) capable of delivering 2.6 J of energy per blow at a frequency of 1500–1700 blows per minute, the penetration rate (a proxy for resistance) into samples of JSC-1A containing ice contents of 0–8% by mass was measured.

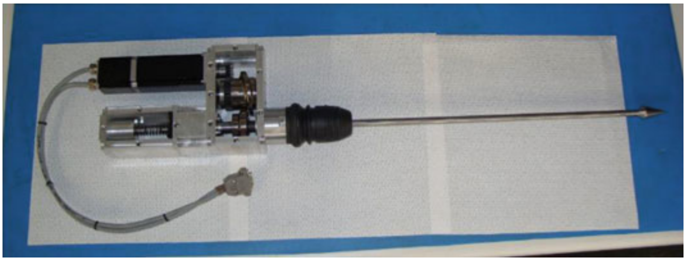

Fig. 15.15 The Honeybee Robotics percussive cone penetrometer. *Source* Mantovani et al. (2016)

Samples were created by mixing JSC-1A with water (in 1% increments) and compacting varying layers into paint cans, followed by an undescribed quick-freezing process to an unknown temperature. Additionally, a 1-m column containing 10 layers of alternating icy/dry simulant was prepared in a similar fashion and frozen to −60 °C (213 K) overnight. Manual penetration of the samples took place outside the freezer in ambient conditions (Fig. 15.16), where some warming of the samples is expected to have occurred. An electronic scale below the samples measured the applied vertical force, and the rate and depth of penetration were determined by analyzing video footage of the tests.

It was noted that the speed of penetration decreased with increased ice content, and that the operator was unable to penetrate the simulant with ice contents of 6% or greater. The observed deeper penetrations into some samples (e.g., one sample of pure 100% ice) is expected to be due to the fact that fractured ice/regolith "chunks" have room to move into the surrounding volume, thus allowing additional penetration. Such a theory might be correlated to the concepts of compression and dilation described in Puech and Foray (2002). Additionally, the penetration rate was not a strong function of downward force and suggests that it could be used as an indication of ice content.

The mechanics of penetration into dry or icy materials is assumed to be quite different, as the grains in frozen soils are unable to rearrange themselves when subjected to stress (and subsequent strain) from a penetrating probe. The apparent transition in these two mechanical states occurs between 3 and 5% of ice by mass in JSC-1A in this particular study. Penetration into a multi-layered column (Fig. 15.17) shows that the interleaving dry layers allow room for particle motion, which facilitates

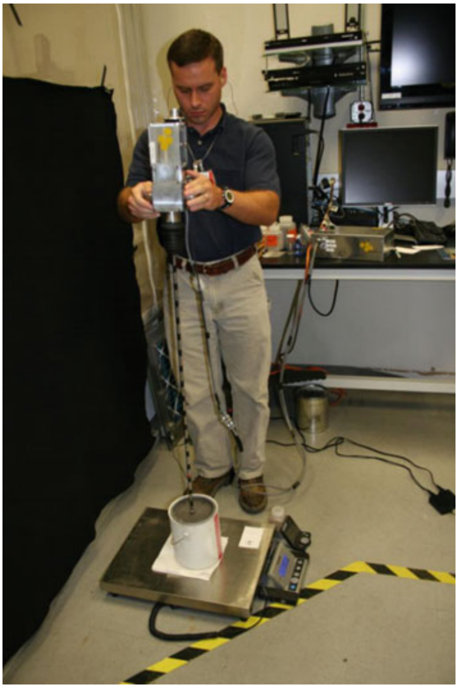

Fig. 15.16 Manual (percussive) cone penetration into a sample can. *Source* Mantovani et al. (2016)

penetration into icy layers that were unable to be penetrated in the previously layered samples (paint cans). It was also noted that, in this case, increased downward force aided penetration as the additional force helped to push fractured material into the surrounding dry material space and create space for the penetrometer to pass.

The experiments, while not well-controlled in terms of experimental conditions, show that a percussive cone penetrometer is capable of penetrating icy regolith at ice contents that a static penetrometer is not, and in a manner insensitive to downward force. Of particular note is the fact that the ultimate penetration depth was not only a function of ice content, but also of the availability of space around the penetrometer tip for relocation of fractured and dislodged material.

Another approach to manual penetration testing was taken by Pitcher et al. (2016), who used both a pencil and a field penetrometer to investigate the properties of icy NU-LHT-2M samples. Preliminary attempts to identify the saturation point of the icy simulant and explore its properties involved mixing six samples of simulant with increasing amounts of water in small (1.34×10^{-4} m^3) containers, which were frozen overnight at −20 °C (253 K). Qualitative measurements of penetration were

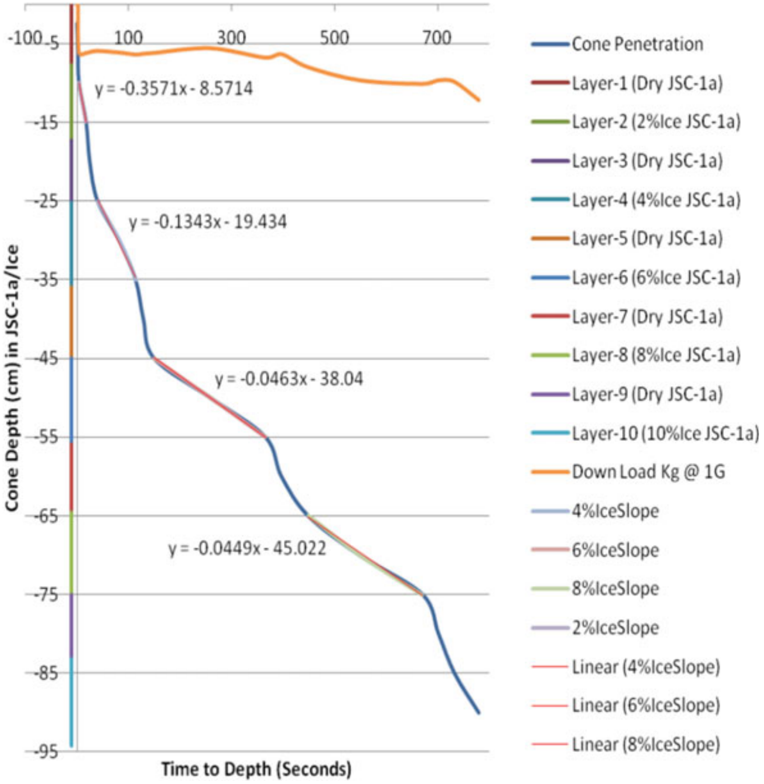

Fig. 15.17 Depth of penetration and down-force as a function of time for a 1-m column, showing interleaving dry layers that allow room for particle motion. *Source* Mantovani et al. (2016)

Fig. 15.18 Six frozen samples of NU-LHT-2M with increasing volumes of water added. Each container has a diameter of 7.2 cm and a height of 3.3 cm. *Source* Pitcher et al. (2016)

performed by pushing a pencil with a 5-mm conical tip into the samples (potentially in ambient conditions) and taking subsequent pictures (Fig. 15.18) to accompany a table of observations.

The qualitative assessment indicated that the frozen regolith experienced a rapid change from ‘soft’ to ‘hard’ when the ice content (water mass) was in the range of 5–9%. To further investigate the rapid change over such a narrow range of ice content, the penetration resistance of icy samples containing 3–4, 4–5, and 7–8% ice was measured (Figs. 15.19 and 15.20). However, useful interpretation of the results is complicated by various uncontrolled experimental factors including the testing temperature, repeated penetrations into single samples, and the creation of subsequently lower ice content samples by allowing a higher moisture sample to dry overnight and be refrozen.

Fig. 15.19 The manual field penetrometer and measurement technique in a frozen NU-LHT-2M sample. *Source* Pitcher et al. (2016)

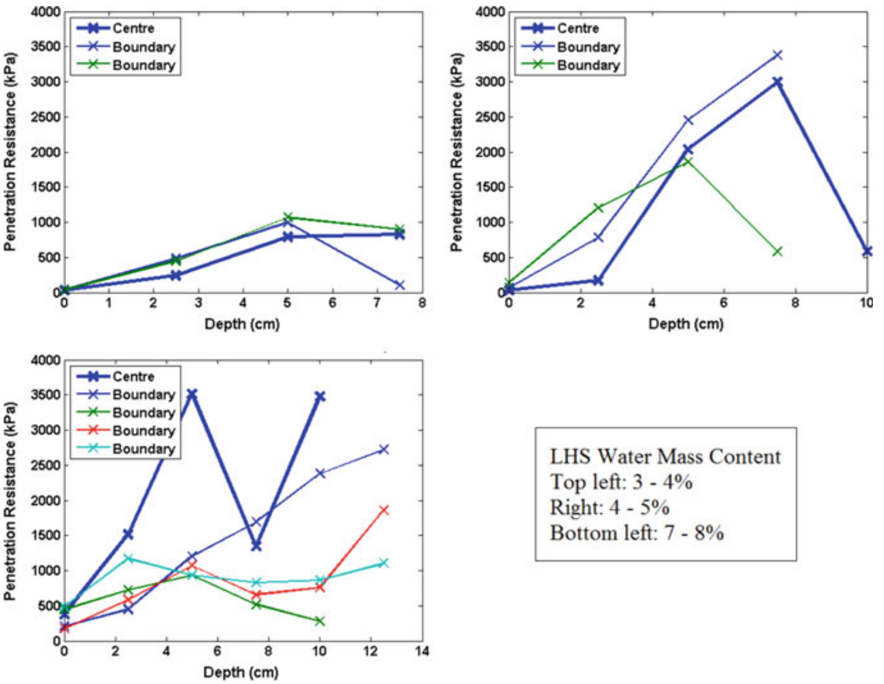

LHS Water Mass Content
Top left: 3 - 4%
Right: 4 - 5%
Bottom left: 7 - 8%

Fig. 15.20 Results of the penetration tests of the frozen NU-LHT-2M sample with different water contents, measuring the resistance experienced by the penetrometer at incremental depths in the sample. *Source* Pitcher et al. (2016)

15.7 Controlled Mechanism

15.7.1 Introduction

Penetration into regolith simulants using a controlled mechanism—that is, an autonomous or semi-autonomous device capable of maintaining a vertical penetration angle with limited deviation, penetrating at a constant rate or maintaining a constant force, and in general controlling as many aspects of the penetration as possible—apparently began with the KOSI experiments (*Kometen-Simulation*) at DLR-Köln in the late 1980s (Kochan et al. 1989 and others). Intended to test comet analogs at cryogenic temperatures, the experiments aimed to help support the eventual Rosetta mission and used a specially designed testing apparatus to penetrate fluffy ice-mineral samples prepared by injection of an aqueous mineral suspension into LN_2.

The testing machinery (Fig. 15.21) consisted of a 5-mm diameter teflon rod with a hemispherical tip fixed to a force gage (piezocone forcemeter) that penetrated at a rate of 0.2 mm/s into the sample. The samples contained H_2O and CO_2 ice (15% by weight) and grains of olivine and montmorillonite of approximately 1 mm (10%

Fig. 15.21 KOSI hardness testing device with cold box and sample. *Source* Kochan et al. (1989)

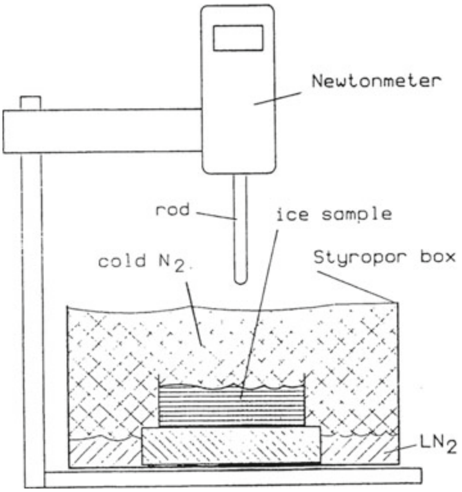

by weight). Of interest is that some icy samples were exposed to solar radiation in a vacuum environment and developed a distinctive crust that was highly resistant to penetration.

Tests were carried out in specially designed boxes and N_2-purged compartments to eliminate atmospheric moisture and maintain sample temperatures that ranged from ~115 K at the near surface to 110 K in the center and 90 K near the underlying cryogenic plate (as shown in Fig. 15.21). In all cases, LN_2 was used as the cooling agent of a baseplate upon which the sample sat to cool, while cold N_2 gas produced by the boiling LN_2 created a cold environment that also served to chill the penetrometer. This is the first example of a system in which the probe temperature was lowered towards that of the sample, though no attempt was made to monitor the temperature of the probe during penetration.

The well-controlled cryogenic tests showed the formation of a hard crust underneath a dusty mantle. While the dusty mantle showed almost no resistance to penetration, the icy crust was highly resistant, and resistance depended on the length of irradiation of the sample. Non-irradiated samples showed an initial parabolic increase to a constant ~200 kPa, while radiated samples demonstrated a ~7 mm thick crust with a strength of up to 1400 kPa, followed by a quick drop to 200–300 kPa below (Fig. 15.22). Samples irradiated for ~41 h maintained a crust of close to 5 MPa strength, almost that of dense crystalline ice at temperature (T) <200 K. The authors attributed the crust formation to three physical processes occurring simultaneously: sublimation, diffusion, and condensation of volatiles in a porous medium.

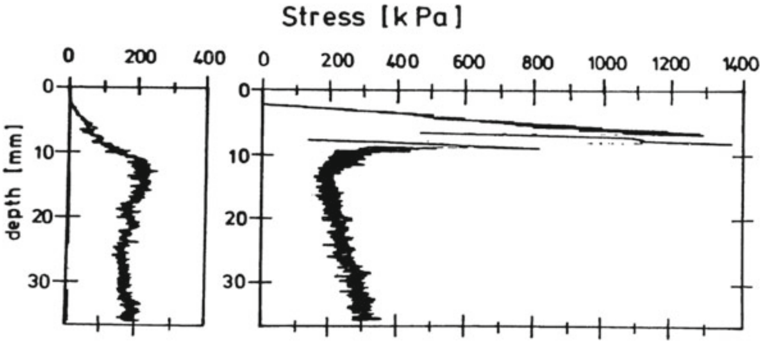

Fig. 15.22 Stress-depth profiles of an unirriadiated (left) and an irradiated (right) model comet, showing the dramatic increase in crustal strength occurring after irradiation. *Source* Kochan et al. (1989)

15.7.2 Indentation

In the early 2000s, Gertsch and colleagues undertook an extensive indentation testing campaign on samples of JSC-1 with water content from <1% to full saturation (>12%) at cryogenic temperatures using an electro-hydraulic closed-loop servo-controlled indentor (Gertsch et al. 2006, 2008). While not precisely penetration tests, they nonetheless provided very useful information on the expected behavior of icy lunar simulant by providing estimates of “specific penetration” and “specific energy” (Teale 1965).

Samples were prepared by mechanically mixing water with fully dried JSC-1 to the desired percentage water content, then compressing the mixtures into 10.9-cm diameter stainless steel test rings at 467 N, intending to simulate the effect of long-term regolith compaction due to meteorite impacts. Samples were then sealed and submersed into LN_2 to cool them to 77 K, as measured by a Type-K thermocouple embedded inside.

Once cooled, the samples were placed into the test machine in ambient conditions (indicating that the samples would be warming continuously). The upper platen of the machine was brought to bear on the sample at 1.24 mm/s, pushing a 19-mm diameter hemispherical indentor vertically into the center of the sample. Once the sample failed—as indicated by measured force drop (Fig. 15.23) or visual confirmation (Fig. 15.24)—the indentor was withdrawn.

Results of the indentation tests indicate that both the specific penetration and specific energy of icy JSC-1 increase with moisture content. Additionally, an apparent change in failure mechanism—identified by subtle changes in failure morphologies and shapes of the load penetration curves—occurs between 1 and 1.3% moisture content and could indicate a transition from brittle to ductile behavior.

Parabolic behavior is again noted with respect to the specific energy of samples near to saturation, while drier samples show a linear relationship between specific energy and water content. Interestingly, the excavated volume (Fig. 15.25) shows a

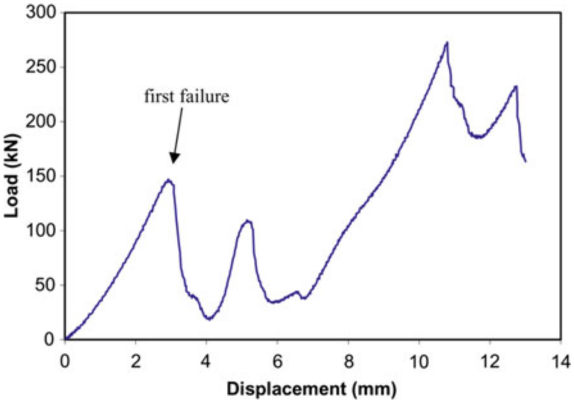

Fig. 15.23 A load penetration (indentation) curve from a 1.48% water content sample of JSC-1, showing multiple failures (load drops) during indentation. *Source* Gertsch et al. (2006)

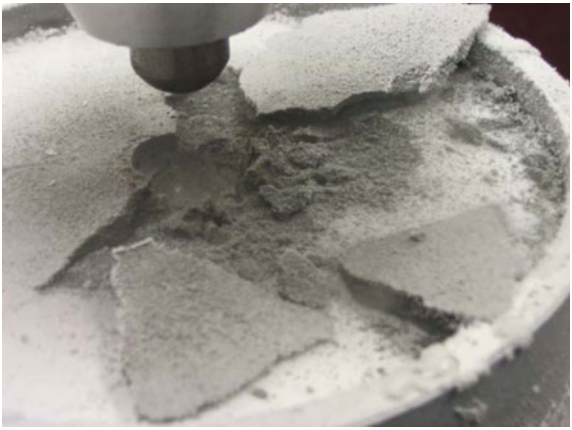

Fig. 15.24 Close view of a sample immediately after indentation, showing some of the chips and the fines produced. *Source* Gertsch et al. (2008)

power law decrease with increasing water content, with a particularly sharp transition between 1 and 3% water content. The authors note that there appears to be a bilinear function between the two regions.

Indentor penetrations into samples of various moisture contents clearly show increased brittle-like behavior with increased saturation (Gertsch et al. 2008). Penetrations into dry JSC-1 proceeded up to 16-mm depth with maximum loads under 5 kN; moist samples (0.6–1.5% water content) experienced depths of 12–14 mm and maximum forces of 15–27 kN; ~8 to 9% samples reached 200 kN at depths of roughly 6 mm; and samples with 10–12% water content behaved like strong sandstone with maximum loads of 200+ kN at 12-mm depth. Additionally, the specific penetration results were used to correlate unconfined compressive strength (UCS) estimates and compared with a single direct UCS measurement at 77 K, yielding an estimated UCS curve that predicts values from <20 MPa for low moisture content to >100 MPa at full saturation (>12% water content).

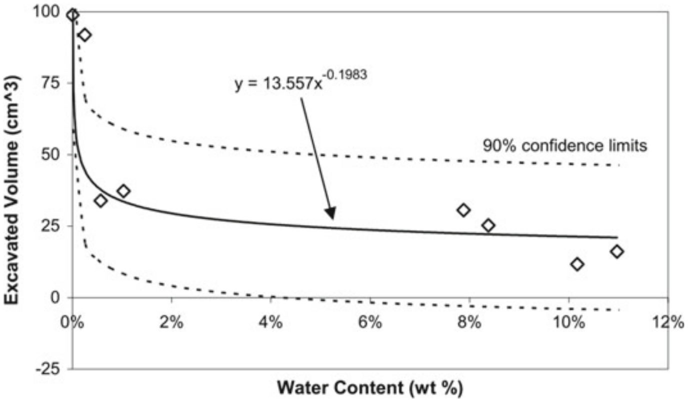

Fig. 15.25 The effect of water content (in JSC-1) on excavated volume, with 90% confidence limits. *Source* Gertsch et al. (2006)

While the authors note that the small number of experiments within the study should be augmented in order to provide details in the transition from ductile to brittle behavior—and in particular the linear or parabolic relationship between specific penetration and moisture content—they were confident in their assessment that at 77 K the icy mixtures behave more like a strong brittle material than a collection of noncohesive dry regolith particles. The transition is explained, according to the authors, by the sharp decrease in the mobility of weak hydrogen bonds in ice as temperature decreases. The reduced mobility increases the strength of the ice content, while the cementing behavior of ice in the unconsolidated granular regolith increases penetration resistance.

15.7.3 Penetration and Relaxation

True penetration tests on lunar simulants using controlled-mechanism penetrometers at both cryogenic and ambient temperatures, vacuum pressures, and dry and saturated states began in earnest only in the last decade. Additional attention to laboratory techniques and cryogenic methods have allowed for more robust explorations of the behavior of simulants at ambient and low-temperature conditions.

In the early 2010s, Kleinhenz and colleagues began a two-phase series of penetration experiments into GRC-3 and NU-LHT-3M simulants at NASA's Glenn Research Center. Using an electric cone penetrometer, they measured the strength, cohesion, friction angle, bulk density, and shear modulus of the simulants at both ambient and vacuum pressure conditions and ambient temperatures in a large sample bed with a depth of 64 cm and a surface area of ~1 m^2, containing 1 ton of simulant. In Phase I, the CPT system was driven by a standard hand drill via a flexible shaft feedthrough into a jackscrew drive, pushing the cone at ~1 cm/s into the simulant of an unknown

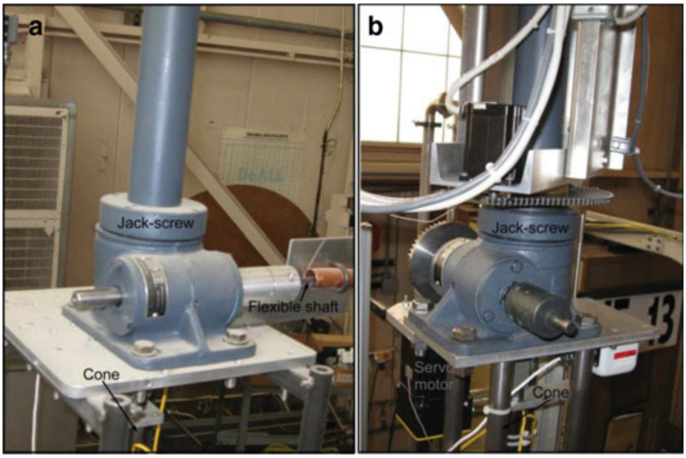

Fig. 15.26 The cone penetrometer drive system during Phase I (**a,** left) and Phase II (**b,** right). *Source* Kleinhenz and Wilkinson (2014)

density(Kleinhenz and Wilkinson, 2012). The pressure at the tip was recorded at 2–5-mm depth intervals, assuming the use of an internal strain gage common to electric penetrometers. Phase II saw the 2.54-cm diameter, 60° mini-electric cone driven by a servomotor (Kleinhenz and Wilkinson 2014) (Fig. 15.26).

Phase I results show the varying relationships of penetration resistance with depth for three penetrations: two in GRC-3 and one in NU-LHT-3M. Parabolic increases were seen most prominently in the NU-LHT-3M test, while the tests on GRC-3 showed undulating variations in resistance with depth that alternate between what appears to be a logarithmic behavior followed by parabolic behavior and may indicate two separate layers. The authors attribute the variation in resistances to both sample preparation technique and consolidation time, suggesting that uncontrolled experimental conditions affected the results. GRC-3 was rapidly pluviated into the bin while NU-LHT-3M was filled by dumping many large 5-gallon buckets. The beds were left to settle for different lengths of time.

Phase II, begun in November 2011, explored variations in pressure (vacuum versus ambient) and NU-LHT-3M simulant bed preparation ("tilled" versus tamping) (Fig. 15.27). Additional variations in the time between tests where sediment consolidation likely occurred create some difficulties in comparing the results, but in general the penetrations show that increased consolidation (increased density) resulted in increased penetration resistance. Interestingly, penetration resistance also appeared to increase with decreasing pressure, though no explanation of the phenomenon is provided.

In 2011, Cil (2011) performed penetrations into the lunar simulant JSC-1A and a simple Ottawa Sand using both a vehicle-mounted penetrometer system and a controlled mini-CPT. The study investigated the effect of cone and specimen size

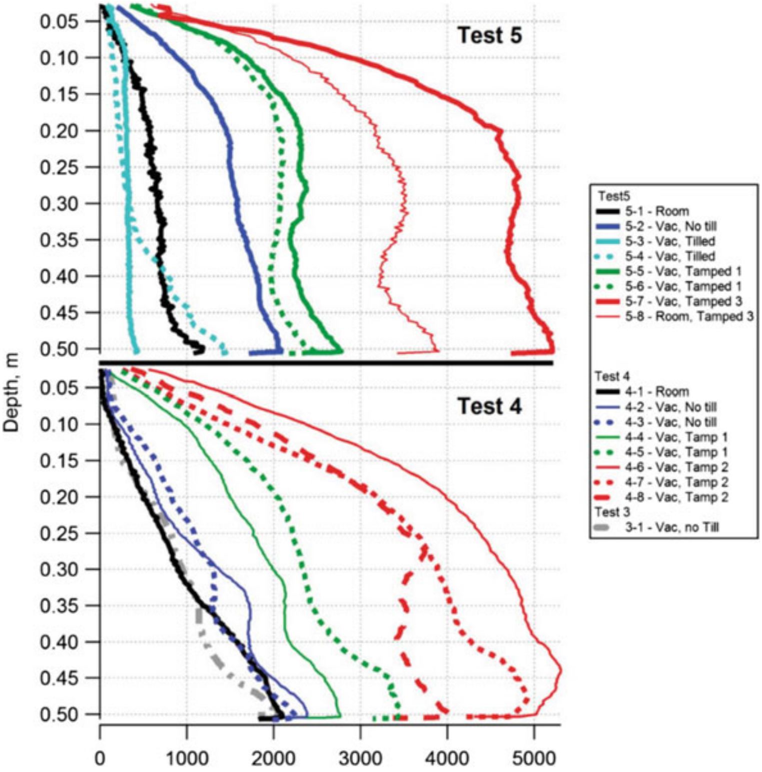

Fig. 15.27 CPT results in NU-LHT-3M, showing multiple tests at both ambient ('Room') and vacuum ('Vac') pressures and at various levels of tamping. An increase in penetration resistance with increased density (increased tamping) is seen, as well as an apparent increase in resistance with decreasing pressure. *Source* Kleinhenz and Wilkinson (2014)

(CCR) on penetration resistance, as well as the effect of boundary conditions on the behavior of the granular analog materials.

Vehicle-mounted penetrations were performed using a 20-ton truck into a cylindrical container 91 cm high and 13.84 cm in diameter, at various densities and pressures. While there is no mention of the probe size, Fig. 15.28 indicates that the CCR was quite low, perhaps on the order of 5. Similarly, no measurements of sample preparation density are provided, only "loose" and "dense". The results of these penetrations show a general parabolic increase with depth, though one test shows the initial nonlinear increase followed by a "plateau" of resistance, similar to that predicted by Puech and Foray (2002) (Fig. 15.29 and Table 15.11). The reliability of these measurements, however, is questionable due to the low CCR, likely boundary effects, and limited number of data points.

Supporting measurements, in particular those providing supplementary data for the subsequent DEM model, were obtained using a controlled mini-CPT in JSC-1A and Ottawa Sand. The mini-CPT had a reported cone diameter of 3.125 mm and

Fig. 15.28 The testing set-up for CPT measurements in JSC-1A, showing the large-diameter truck-mounted penetrometer and the relatively narrow cylindrical testing container. *Source* Cil (2011)

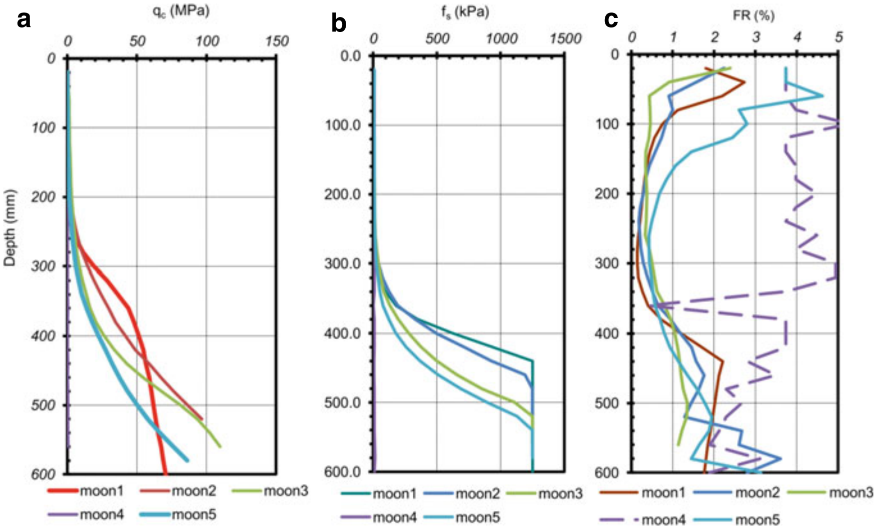

Fig. 15.29 Results of CPT measurements in JSC-1A showing tip resistance (**a**, left), sleeve friction (**b**, middle), and friction ratio (**c**, right). *Source* Cil (2011)

Table 15.11 Summary of field CPT experiments in JSC-1A. Modified from Cil (2011)

Experiment	Soil height before penetration [mm]	Soil height after penetration [mm]	Dry density [g/cm^3]	Pressure source
Moon1	726.4	Not recorded	1.78	Atmospheric
Moon2	706.1	Not recorded	1.78	Atmospheric
Moon3	709.9	571.5	1.78	+25 kPa
Moon4	769.6	670.5	1.75	−25 kPa
Moon5	607.1	Broken	1.75	−25 kPa

penetrations were performed in cylindrical containers of 25.4 and 40.5 mm radius, both 101.6 mm in height, giving CCRs of 8 and 13 respectively and suggesting that edge effects could influence results (Fig. 15.30). Sample preparation was noted as being the most challenging aspect of the experiment, and relatively little information on the resulting sample densities is provided. "Loose" samples were prepared by free-pouring simulant from a specified height through a funnel followed by vibratory compaction to a pre-determined surface level (back-calculated from the desired density), and "dense" samples were formed in three layers using a standard Proctor Method. Samples were loaded into a GeoJack machine, and penetration occurred at ~10 mm/min (0.17 mm/s), while a load cell-recorded resistance and displacement of the probe was measured with an LVDT sensor.

Results of multiple penetrations into both materials showed that penetration resistance increases drastically for low void-ratio samples and that high void-ratio samples see either a linear increase in resistance with depth or, in some cases, an initial

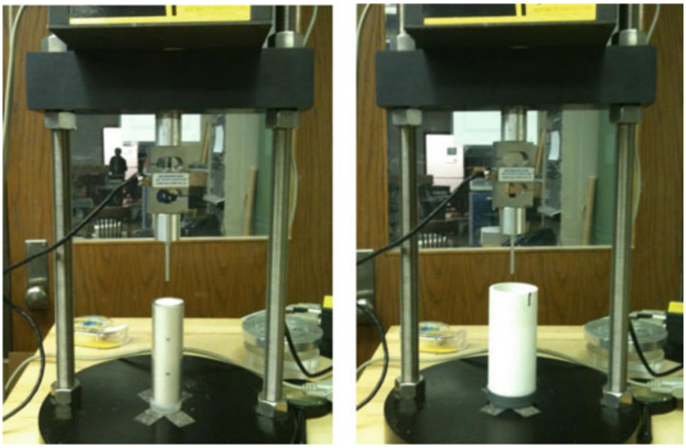

Fig. 15.30 Mini-CPT experimental set-up for supplementary input to a discrete-element model. Note the small penetrometer diameter but narrow container diameter (left) compared to the larger container (right). *Source* Cil (2011)

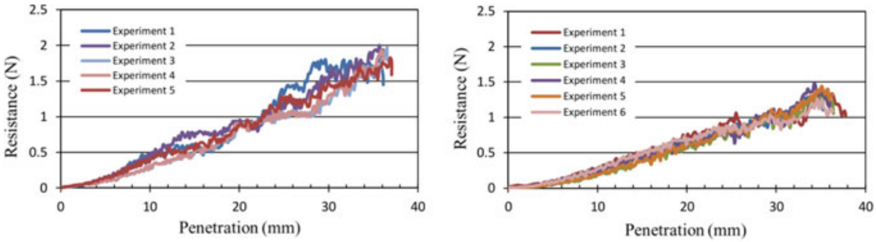

(a) Ottawa sand in container A with loose condition

(c) Ottawa sand in container B with loose condition

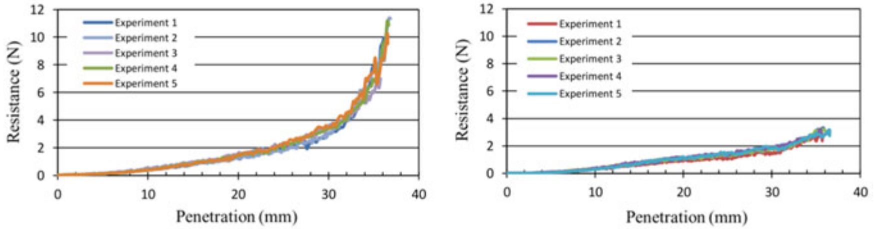

(b) Ottawa sand in container A with dense condition

(d) Ottawa sand in container B with dense condition

Fig. 15.31 Mini-CPT results in Ottawa Sand with dense and loose density conditions in the small (container A) and large (container B) containers. *Source* Cil (2011)

parabolic increase followed by a sustained constant force (similar to that predicted by Puech and Foray, 2002) (Figs. 15.31 and 15.32).

Cil (2011) claims that the variability seen in the penetration resistance of JSC-1A is due to inherent heterogeneity in identically prepared samples, a result of the simulants' particle-size distribution (as compared to that of Ottawa Sand). Furthermore, the sharp increase in resistance with depth (occurring at ~27 mm) in the "dense" condition for both materials is likely due to edge effects, observed to be most pronounced in the narrow container (A), and is a function of high particle confinement and particle interlocking. The plateau state achieved by JSC-1A in a dense condition and in the larger container (B) is taken as an indication that the soil boundary conditions have been removed. Ultimately, the experiments demonstrate the sensitivity of penetration resistance to sample density and container size (boundary effects), though various aspects of the penetration behavior (such as the flattening of the dense JSC-1A in the large container at depths > 20 mm while Ottawa Sand follows a predicted increase) remain unaddressed.

In 2014, Seweryn et al. (2014) proposed the use of a low-velocity penetrometer (LVP) for determining the geotechnical properties of regolith, in a method similar to a dynamic cone penetrometer but modified for use in space (low mass, low power). LVPs are penetrators that utilize low velocity, high stroke energy, and low power to autonomously generate forward motion in zero- or micro-gravity, and are designed to carry various sensors for in-situ investigations of planetary subsurfaces. Other examples of LVPs (Fig. 15.33) are the MUPUS system used on the Philae lander, the mole KRET, the CHOMIK, and the HP3 device used on the Mars InSight mission.

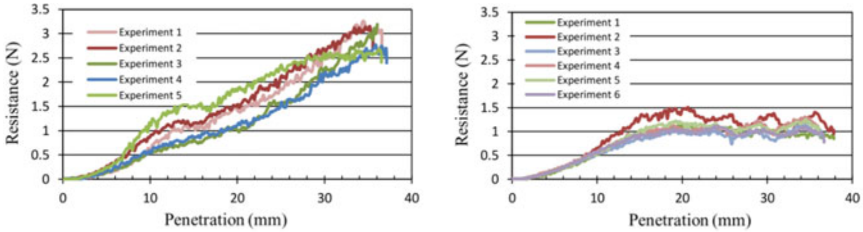

(a) JSC-1A simulant in container A with loose condition (c) JSC-1A simulant in container B with loose condition

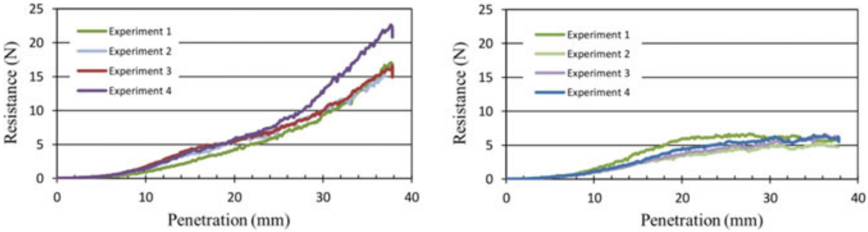

(b) JSC-1A simulant in container A with dense condition (d) JSC-1A simulant in container B with dense condition

Fig. 15.32 Mini-CPT results in JSC-1A with dense and loose density conditions in the small (container A) and large (container B) containers. *Source* Cil (2011)

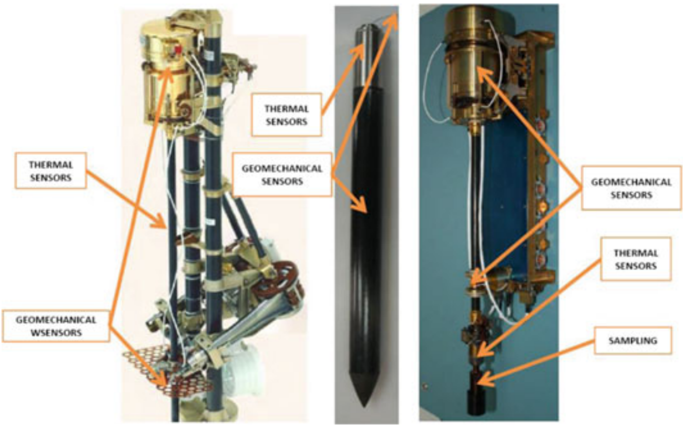

Fig. 15.33 Examples of the LVP devices. Left: the MUPUS instrument (Rosetta mission to comet 67P). Middle: the mole KRET penetrator. Right: the CHOMIK instrument (Phobos Grunt mission). *Source* Seweryn et al. (2014)

Results from penetration into lunar regolith simulants (AGK 2010 and a dry quartz simulant) using the KRET penetrometer show the expected increasing resistance with increased density (noted as “not compacted”to “highly compacted”), as indicated by the decreasing depth per stroke (DPI—dynamic cone penetration [DCP] penetration index) in Fig. 15.34 and the shallower penetration depth of the penetrometer tip (Fig. 15.35) for highly compacted simulant.

A robust exploration of the penetration response of dry and icy lunar regolith simulants under controlled laboratory conditions—at variations in density, moisture content, pressure, and temperature—was performed beginning in 2019 by J. Atkinson during doctoral studies at the Center for Space Resources at the Colorado School

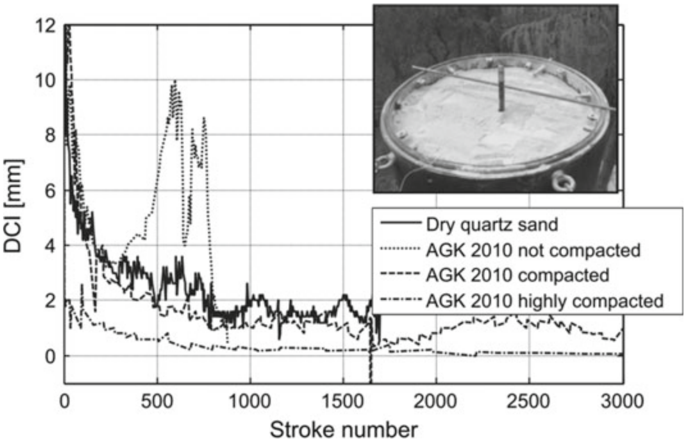

Fig. 15.34 A comparison of the DPI (DCP penetration index) parameters obtained using the KRET device in lunar simulant AGK 2010 under various compaction conditions, as well as in dry quartz sand. *Source* Seweryn et al. (2014)

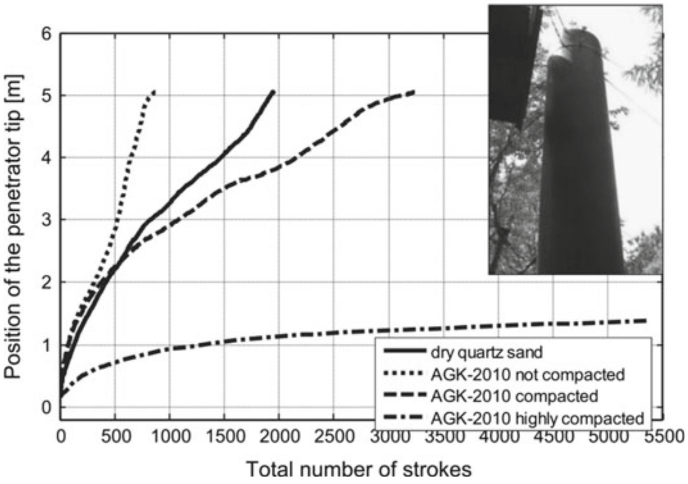

Fig. 15.35 A comparison of the depth of penetration to total number of strokes obtained using the KRET device in lunar simulant AGK 2010 under different compaction conditions, as well as in dry quartz sand. *Source* Seweryn et al. (2014)

of Mines. A specially designed penetrometer capable of making high-resolution measurements of force and depth (Dreyer et al. 2018) allowed for precise monitoring of not only the penetration behavior of the simulants, but the relaxation of the granular material after initial penetration as well. The relaxation behavior of penetrated granular materials (especially simulants) had not yet been studied and appears to be sensitive to geotechnical and environmental conditions that the penetration resistance is insensitive to.

Both dry and cryogenic testing of lunar regolith simulants utilized the ISRU Experimental Probe (IEP) (Fig. 15.36), a 6-mm diameter, 30° conical controlled-mechanism penetrometer capable of penetrating simulant samples to a depth of ~30 mm. Vertical motion was driven by a lead screw such that, when under load, the backlash (reactive movement) was negligible and continuous monitoring of the force at the probe tip using a mounted force gage allowed the relaxation of the simulant around the probe tip to be observed and measured. Cryogenic tests were performed under ambient and vacuum conditions at sample temperatures of ~110 K, while dry tests were performed at similar pressures and elevated temperatures typically approaching 323 K, both at a rate of 0.25 mm/s.

Atkinson et al. (2019) performed 24 penetration tests on dry GRC-3 and JSC-1A at low (~20%) and high (80%) relative densities at pressures of ~700 and ~0.05 Torr. Samples were prepared using both standard Proctor and vibratory compaction methods to relatively high degrees of density accuracy via specially designed compaction sleeves. Final sample containers measured 9.4 cm in diameter and 7.3 cm in depth, giving a CCR of ~16. The depth of penetration (30 mm) was

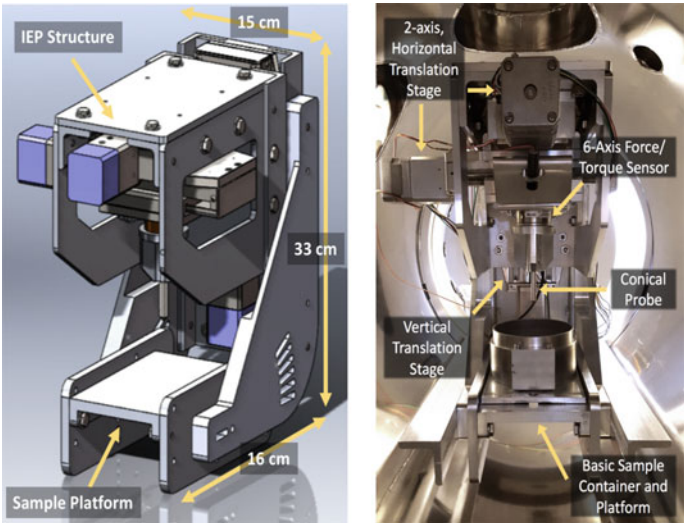

Fig. 15.36 The ISRU Experimental Probe (IEP). Left: CAD model. Right: IEP with a basic sample container inside a vacuum chamber. *Source* Dreyer et al. (2018)

less than half the container depth in order to minimize boundary effects from the sample base.

Dry penetration curves (Fig. 15.37) were fitted with a parabolic equation $\left(F(z) = \alpha z + \beta z^2\right)$, as described in Sect. 15.3.2. Low-density samples (~20% relative density) showed a steady, nonlinear increase in resistance with depth—to ~5 N at 30-mm depth—while high-density samples (80% relative density) displayed a more dramatic nonlinear increase with depth to reach resistances of 20 N or more. The coefficient of the parabolic equation β shows high sensitivity to density and relative insensitivity to pressure (Fig. 15.37), is shown to be related to the model developed by Puech and Foray (2002), and gives moderate approximations of basic geotechnical properties such as bearing capacity and lateral slip line length. The linear penetration coefficient α, while displaying some correlation to geotechnical parameters, shows high volatility since higher-density samples demonstrate essentially parabolic penetration behavior with little to no linear component. Despite the high CCR, potential edge effects were identified at depths >20 mm by the onset of z^3 behavior.

Dry relaxation curves were fitted with a Maxwell-style rheological model (Sect. 5.3) whose parameters correspond to both the elastic (k_i) and viscous (τ_i) behavior in relaxing granular materials. Of particular importance is that the relaxation behavior showed significant sensitivity not only to sample density but to the simulant type and testing pressure (Fig. 15.38), predominantly the elastic coefficients k_i. Some sensitivities are non-unique as evidenced by the parameter k_1, which decreases in value with both increasing density and pressure, in which case comparison to other parameters (such as β, sensitive only to density) can be used to determine the testing condition. Both elastic parameters k_e and k_1 are sensitive to simulant type, likely due to the increased angularity of JSC-1A inhibiting grain rotation and increasing the interlocking of grains leading to both a higher residual supported load (k_e) and a delayed onset of relaxation (k_1).

The increased cohesion in JSC-1A (Li et al. 2013) was also potentially observed in the relaxation behavior of both simulants to their coarse-grained (250–710 μm) and fine-grained (<75 μm) versions, sieved in house. Figure 15.39 shows that JSC-1A—with its full combination of all particle sizes in its original particle-size distribution—shows more cohesive behavior (as evidenced by the relaxation parameter k_e which relates to the external Hookean spring in Sect. 15.3.3) than either the fine or coarse versions. This phenomenon was predicted by Sanchez and Scheeres (2012) for application to the cohesive nature of rubble-pile asteroids, in which the cohesion is created through the interaction of many small particles with nearby larger ones, thus requiring a distribution of particle sizes for increased cohesion. GRC-3, a cohesionless sand, has a k_e at full particle-size distribution that appears to be a volumetric average of those of its fine and coarse versions.

The same models of nonlinear penetration and Maxwellian relaxation behavior were used to describe the results of similar penetration tests conducted on icy JSC-1A samples at cryogenic temperatures. A specially designed cryogenic cooling reservoir (Fig. 15.40) kept the sample at ~110 ± 20 K while the probe was cooled to ~188–211 K (as measured using an internally embedded Type-K thermocouple). The cryogenic cooler allowed for pre-cooling of the samples in LN_2 outside the

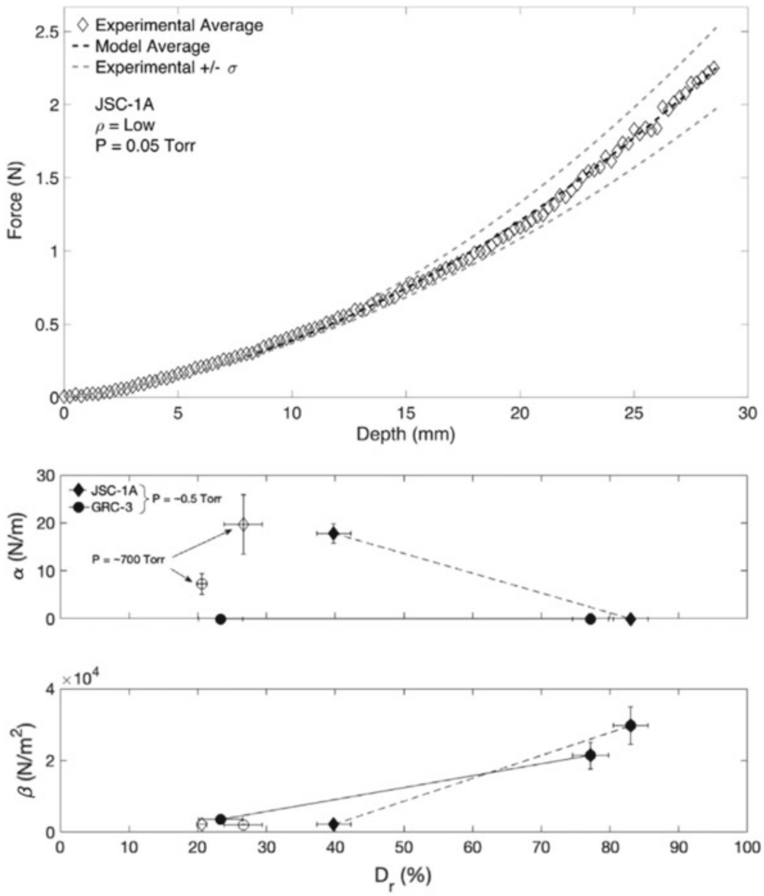

Fig. 15.37 Top: A sample penetration curve from a low-density JSC-1A tested at 0.05 Torr showing the experimental average (diamond markers) and one standard deviation (dashed gray line), with the associated model fit (dashed black line). Middle and Bottom: α (N/m) and β (N/m^2) model values plotted against relative density (%) for all six full particle distribution tests. JSC-1A tests are represented as diamonds and GRC-3 as circles. Black markers are tested at ~0.5 Torr, white markers at ~700 Torr. Error bars are taken from the model fits to the standard deviation curves and thus represent experimental variability. *Source* Atkinson et al. (2019)

vacuum chamber before insertion and for free flow of LN_2 through the reservoir while in the vacuum to minimize heat gain and maximize cooling rate.

Twenty-four penetration tests into samples of JSC-1A at densities of 1.55–1.63 g/cm^3 and levels of saturation from 0 to 12% (including one sample of pure water ice) using the same IEP device (Dreyer et al. 2018), modified to handle cryogenic temperatures, resulted in both penetration and relaxation curves that were strongly sensitive to ice content.

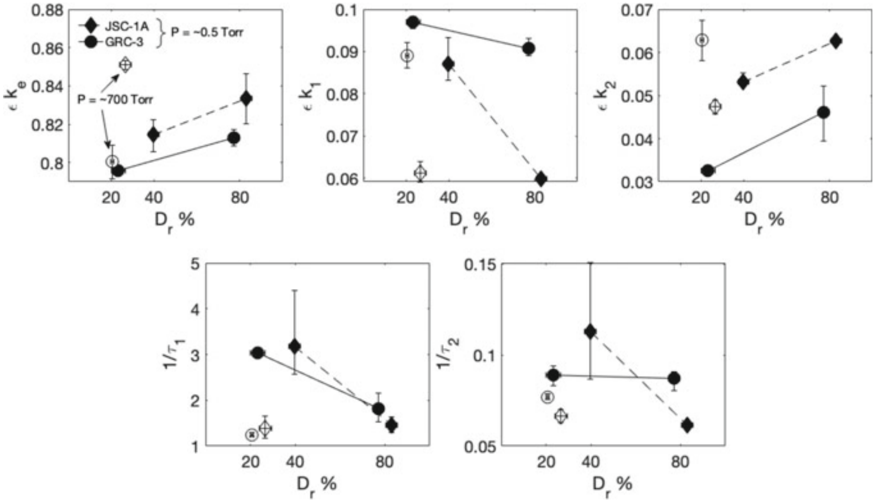

Fig. 15.38 Model parameter values versus relative density for all full particle distribution tests. JSC-1A tests are represented as diamonds and GRC-3 as circles. Black markers indicate testing at 0.05 Torr while open markers indicate testing at ~700 Torr. Error bars are taken from the model fits to the standard deviation curves and thus represent experimental variability. Elastic parameters are at the top while time-dependent parameters are at the bottom. k_1 is the only parameter capable of distinguishing simulant type, test pressure, and sample density. *Source* Atkinson et al. (2019)

Cryogenic penetration curves (Fig. 15.41) followed a parabolic increase for higher ice content samples (≥1%) and linear responses for low ice content (<1%). Full penetration to ~30 mm was only possible for samples <1% ice content, as the 120 N maximum threshold for the machine was achieved at shallow depths for higher ice contents. A step change in penetration resistance (similar to that seen by both Gertsch et al. 2006 and Pitcher et al. 2016) appears between 1 and 3% ice content. The phenomenon is explained by the authors to parallel percolation theory: it is the result of the progressive filling of pore space within the simulant to the point at which the pore ice (~35% content) can begin to act as an interconnected, load-bearing component, thus increasing the resistance to vertical force. Below this point, the majority of the load is still borne by the grains with cementing assistance from the distributed pore ice (Fig. 15.42). Since the phenomenon is dependent on the pore-size (and thus pore-volume) distribution, it would be expected to result in a step change at different percentages of ice content, which may explain the identification of such a step change at between 5 and 9% ice content in NU-LHT-2 M (Pitcher et al. 2016).

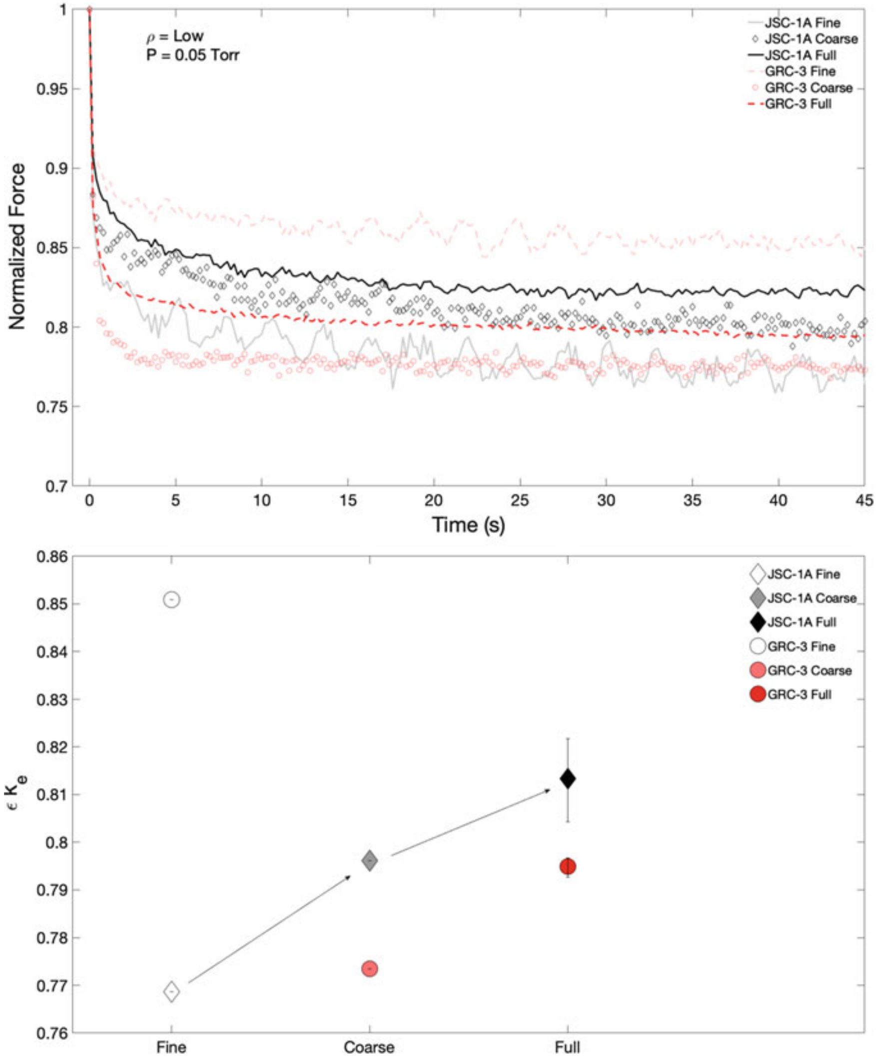

Fig. 15.39 Relaxation curves (note linear time) of fine, coarse, and full particle-size distribution JSC-1A and GRC-3. Bottom: Distribution of relaxation parameter k_e for the associated fine, coarse, and full JSC-1A (diamonds) and GRC-3 (circles) tests. *Source* Atkinson et al. (2019)

The model parameters for both penetration (α and β) and for relaxation (elastic parameters k_i) were sensitive to ice content (Figs. 15.43 and 15.44), with the relationships taking the forms

$$\alpha = 1162p_{ice} + 147.5p_{ice}^2, \tag{15.10}$$

$$\beta = 1E6p_{ice}^2, \tag{15.11}$$

$$k_e = 0.935\left(p_{ice}^{0.013}\right), \tag{15.12}$$

$$k_1 = 0.054\left(e^{-0.28p_{ice}}\right), \tag{15.13}$$

$$k_2 = 0.028\left(p_{ice}^{-0.096}\right), \tag{15.14}$$

where p_{ice} is the sample ice content expressed as a percentage.

Additionally, the relaxation behavior showed sensitivity to temperature, as evidenced by the increase in k_e value for dry (0%) JSC-1A tested at 110 K compared to that tested at 320 K in Atkinson et al. (2019). Consequently, this modified penetrometer has shown the potential for identifying simulant type, cohesion, density and

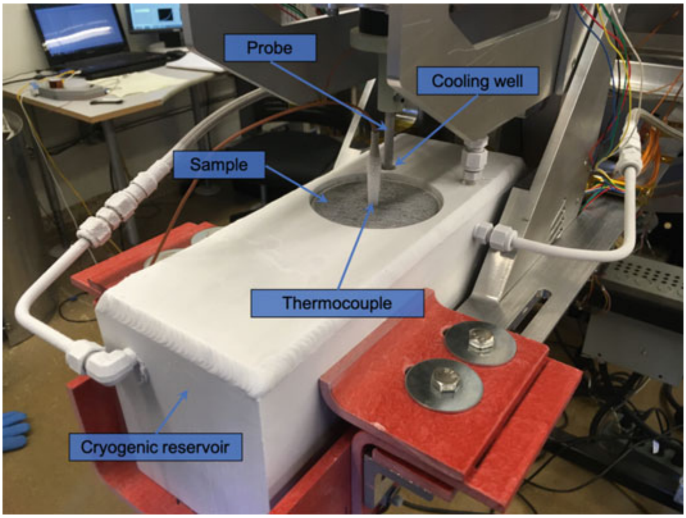

Fig. 15.40 The cryogenic cooler as seen connected into a specialized garolite cradle beneath the IEP penetrometer. Inlet and outlet hoses provide circulation of liquid nitrogen, as the cooler is hollow to create a cooling, stable reservoir surrounding the sample. The probe itself is seen pressed into the cooling well (at back), while a thermocouple is embedded in the sample center for temperature monitoring during thermal tests. *Source* Atkinson et al. (2019)

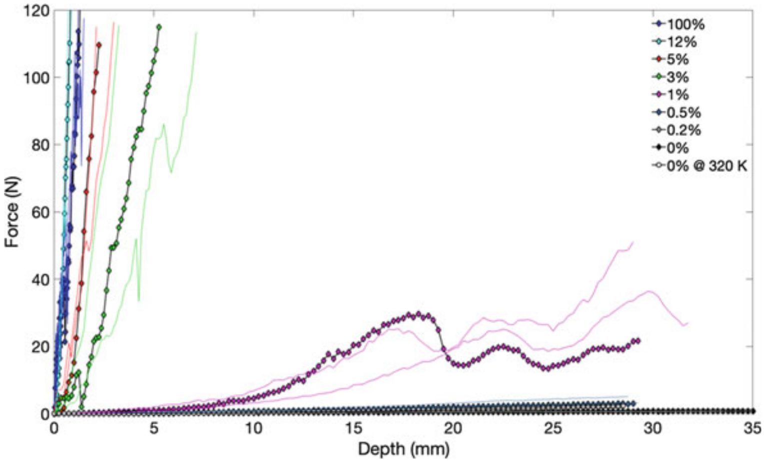

Fig. 15.41 Penetration curves for all ice contents showing resistance force as a function of probe depth, including a test of 0% at 320 K from Atkinson et al. (2019). All tests performed at ~110 K unless otherwise noted. Markers indicate one of three runs at the same ice content, while solid lines indicate the other two. *Source* Atkinson et al. (2019)

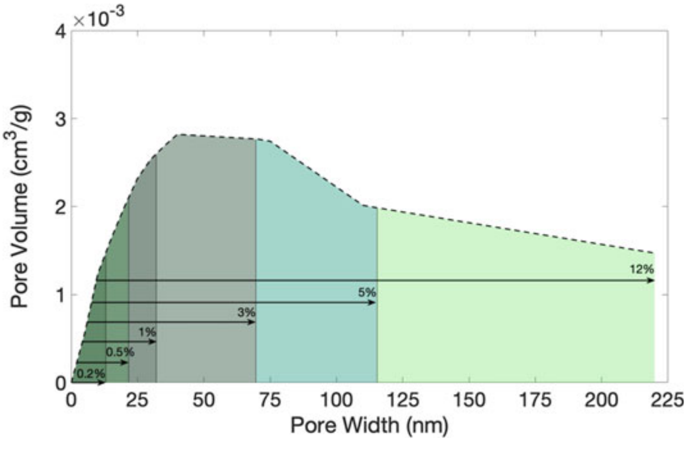

Fig. 15.42 Nitrogen adsorption analysis of JSC-1A, showing pore volume as a function of pore width. Arrows indicate the direction of pore filling (from smallest pores to largest) at each identified moisture content (%). Colors indicate the additional pore space and pore volume fluid filled at each associated moisture content. From Atkinson et al. (2020)

test pressure at ambient to elevated temperatures, and temperature and ice content at cryogenic conditions.

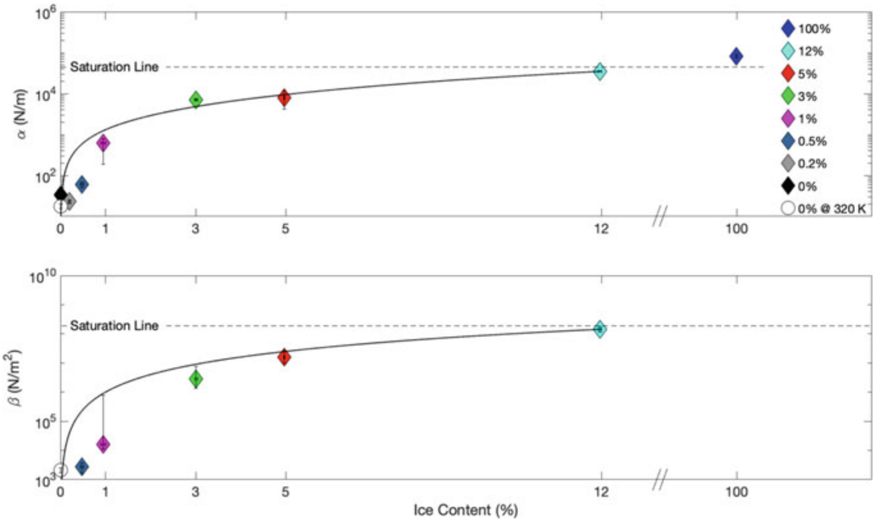

Fig. 15.43 Coefficients of the second-order model fits to penetration curves α (top) and β (bottom) as a function of ice content. Note the nonlinear increase in value for both coefficients to a saturated limit. β values at 0, 0.2, and 100% ice content are zero and therefore not displayed on the semi-log axis. All tests performed at ~110 K unless otherwise noted. Note that horizontal error bars indicating the range in ice content are present but extremely small. *Source* Atkinson et al. (2020)

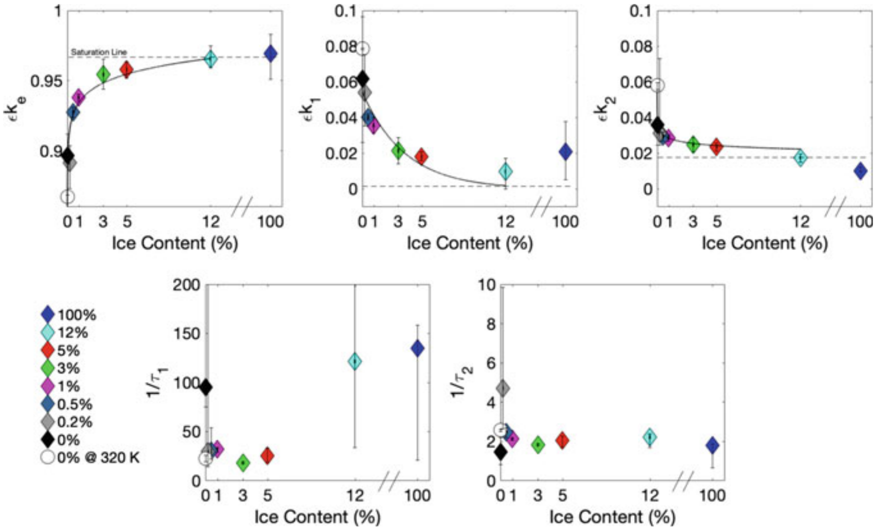

Fig. 15.44 Parameters of the two-arm Maxwell model fits to relaxation curves in the initial 1 s of relaxation as a function of ice content. Note the nonlinear increase in k_e and decrease in k_1 and k_2 to a saturated limit. All tests performed at ~110 K unless otherwise noted. *Source* Atkinson et al. (2020)

15.7.4 Synthesis

Penetrometer tests in lunar simulants, while relatively limited in number and performed in a wide range of environmental conditions using varied experimental methods, have nonetheless provided insight into the possible behavior and characteristics of both dry and icy lunar regolith.

Apollo-era researchers performed both penetrations into small amounts of returned lunar regolith and larger tests in more widely available lunar simulants and other granular materials. They determined that penetration resistance and its rate of change with depth are indicators of soil density and decrease with gravity. The research indicated generally linear increases in penetration resistance with depth, with minor evidence of nonlinearity.

More recent research has involved the use of both manual field and controlled-mechanism penetrometers into simulants containing water ice from zero to full saturation, and at temperatures and pressures approaching those expected in situ. Wide ranges in the experimental methods have led to difficulties in interpreting data in some cases, though in general there is ample evidence of nonlinear relationships between penetration resistance and depth (contrary to established analytical solutions). It should be noted, however, that the boundary effects induced by the bottom boundary of sample containers has not been quantified in sufficient detail.

Evidence also points to the sensitivity of the penetrometer to general soil properties like density, with a particular emphasis in this regard on the ice content of the simulants at low temperatures (reaching cryogenic in some cases). Increases in ice content correspond to nonlinear increases in penetration resistance, with large step changes in resistance potentially a result of the amount and distribution of ice in the granular matrix.

In addition to relative density and ice content, the relaxation of the granular material after penetration shows sensitivity to various bulk granular properties such as cohesion and grain angularity, as well as experimental conditions such as pressure and temperature.

The use of the penetrometer in exploring the characteristics and behavior of granular materials at a more detailed level than previously pursued should become a focus for researchers in the future. This simple device, robust enough to be deployed on the lunar surface and adaptable enough to perform highly technical tests in the laboratory, has unexplored potential both as a primary instrument in future missions and as a terrestrial investigative tool for more advanced soil research.

15.8 Permissions

Figure 15.1: Reprinted from M.B. Kirkham, *Principles of Soil and Plant Water Relations* (2014), 171–183 with permission from Elsevier.

Figure 15.2: Reproduced by permission of ERDC.

Figure 15.3: Approved for public release; dstribution is unlimited.

Figure 15.4: Reprinted from Atkinson et al., Penetration and relaxation behavior of dry lunar regolith simulants (2019), *Icarus,* 328, 82–92 with permission from Elsevier.

Figures 15.5–15.7, 15.9: Reproduced by permission of the Lunar and Planetary Institute, Houston.

Figure 15.8: Reprinted from Ray et al., JSC-1A lunar soil simulant: Characterization, glass formation, and selected glass properties (2010), *Journal of Non-Crystalline Solids*, 356, 2369–2374 with permission from Elsevier.

Figure 15.10: Reprinted from Houston & Namiq, Penetration resistance of lunar soils (1971), *Journal of Terramechanics*, 8, 59–69 with permission from Elsevier.

Figures 15.11, 15.16–16.17, 15.26–15.27: Reproduced by permission of NASA.

Figures 15.12–15.14: Reproduced by permission of Heather Oravec.

Figure 15.15: Reproduced by permission of Honeybee Robotics.

Figures 15.18–15.20: Reproduced by permission of COSPAR.

Figures 15.21–15.22: Reproduced by permission of Harald Hellman.

Figures 15.23, 15.25: Reproduced from Gertsch et al., Effect of water ice content on excavatability of lunar regolith (2006) with permission from Missouri University of Science and Technology.

Figure 15.24: Reproduced from Gertsch et al., *Review of Lunar Regolith Properties for Design of Low Power Lunar Excavators* (2008) with permission from AIP Publishing.

Figures 15.28–15.32: Reproduced by permission of Mehmet Cil.

Figures 15.33–15.35: Reprinted from Seweryn et al., Determining the geotechnical properties of planetary regolith using Low Velocity Penetrometers (2014), *Planetary and Space Science*, 99, 70–83 with permission from Elsevier.

Figure 15.36: Reprinted from Dreyer et al., A new experimental capability for the study of regolith surface physical properties to support science, space exploration, and in situ resource utilization (ISRU) (2018), *Review of Scientific Instruments*, 89, with the permission of AIP Publishing.

Figures 15.37–15.39: Reprinted from, Atkinson et al., Penetration and relaxation behavior of dry lunar regolith simulants (2019), *Icarus,* 328, 82–92 with permission from Elsevier.

Figures 15.40–15.44: Reprinted from Atkinson et al., Penetration and relaxation behavior of JSC-1A lunar regolith simulant under cryogenic conditions (2020), *Icarus,* 346, 113,812 with permission from Elsevier.

References

Alshibli, K.A., and A. Hasan. 2009. Strength properties of JSC-1A lunar regolith simulant. *J Geotech Geoenvironmental Engineering* 135 (5): 673–679. https://doi.org/10.1061/(ASCE)GT.1943-5606.0000068.

Atkinson, J., et al. 2019. Penetration and relaxation behavior of dry lunar regolith simulants. *Icarus* 328: 82–92. https://doi.org/10.1016/j.icarus.2019.03.009.

Atkinson, J., et al. 2020. Penetration and relaxation behavior of JSC-1A lunar regolith simulant under cryogenic conditions. Icarus 346(113812). https://doi.org/10.1016/j.icarus.2020.113812.

Bekker, M. G. 1969. *Introduction to Terrain—Vehicle Systems,* 1st ed. University of Michigan Press.

Blok, C., et al. 2019. *Analytical methods used with soilless substrates,* 2nd ed. Soilless culture. Elsevier B.V. https://doi.org/10.1016/b978-0-444-63696-6.00011-6.

Butlanska, J., et al. 2012. Multi-scale analysis of cone penetration test (CPT) in a virtual calibration chamber. *Canadian Geotechnical Journal* (December): 1–26. https://doi.org/10.1139/Published.

Carrier, W.D.I., L. G. Bromwell, and R.T. Martin. 1972. Strength and compressibilty of returned lunar soil. In *Proceedings of the 3rd lunar science conference,* 3223–3234. The MIT Press.

Carrier, W.D.I., L.G. Bromwell, and R.T. Martin. 1973. Behavior of returned lunar soil in a vacuum. *Journal of the Soil Mechanics and Foundations Division* 99: 979–996.

Carrier, W.D.I., G.R. Olhoeft, and W. Mendell. 1991. Physical properties of the lunar surface. In *Lunar sourcebook*, ed. G.H. Heiken, D.T. Vaniman, and B.M. French, 475–594. New York: Cambridge University Press.

Cherkasov, I. I., and V. V. Shvarev. 1973. Soviet investigations of the mechanics of lunar soils. *Soil Mechanics and Foundation Engineering* 10 (4): 252–256. https://doi.org/10.1007/BF01704945.

Cil, M. B. 2011. *Discrete element modeling of cone penetration in JSC-1A lunar regolith simulant*. Louisiana State University.

Costes, N. C., et al. 1969. *Apollo 11 soil mechanics investigation.* Apollo 11 Preliminary Science Report.

Costes, N. C., G. T. Cohron, and D. C. Moss. 1971. Cone penetration resistance test-an approach to evaluating in-place strength and packing characteristics of lunar soils. In *Lunar and planetary science conference proceedings*, 1973–1987.

Costes, N. C., J. E. Farmer, E. B. George. 1972. *Mobility performance of the lunar roving vehicle: terrestrial studies—Apollo 15 results.* Washington, DC.

Department of the Army Corps of Engineers Mississippi River Commission (1948) *Trafficability of soils: Laboratory tests to determine effects of moisture content and density variations.* Vicksburg, Mississippi.

Dreyer, C.B., et al. 2018. A new experimental capability for the study of regolith surface physical properties to support science, space exploration, and in situ resource utilization (ISRU). *Review of Scientific Instruments* 89 (6): 064502. https://doi.org/10.1063/1.5023112.

Durgunoglu, H. T., and J. K. Mitchell. 1973. *Static penetration resistance of soils.*

ElShafie, A. 2012. Penetration forces for subsurface regolith probes. Theses and Dissertations, University of Arkansas, Fayetteville. http://scholarworks.uark.edu/etd/574%0AThis.

ElShafie, A., and V. F. Chevrier. 2014. Reanalysis of the penetration data provided by Lunokhod rover on the moon. In *45th lunar and planetary science conference proceedings*, February, 31–33. http://adsabs.harvard.edu/abs/2014LPI....45.1533E.

ElShafie, A., V.F. Chevrier, and N. Dennis. 2012. Application of planetary analog mechanical properties to subsurface geological investigations. *Planetary and Space Science. Elsevier* 73 (1): 224–232. https://doi.org/10.1016/j.pss.2012.09.001.

Gertsch, L., R. Gustafson, and R. Gertsch. 2006. Effect of water ice content on excavatability of lunar regolith. *Faculty Research & Creative Works* 10 (1063/1): 2169290.

Gertsch, L., Rostami, J., and R. Gustafson. 2008. Review of lunar regolith properties for design of low power lunar excavators. In *6th international conference on case histories in geotechnical engineering*. Arlington, VA, 1–15.

Green, A. J., and K.-J. Melzer. 1971. *Performance of boeing LRV wheels in a lunar soil simulant*.

Gromov, V.V. 1998. Physical and mechanical properties of lunar and planetary soils. *Earth, Moon, and Planets* 80 (1/3): 51–72. https://doi.org/10.1023/A:1006353510204.

Harr, M.E. 1977. *Mechanics of particulate media.* McGraw-Hill.

He, C., X. Zeng, and A. Wilkinson. 2011. Geotechnical properties of GRC-3 lunar simulant. *Journal of Aerospace Engineering* 421 (July): 123. https://doi.org/10.1061/(ASCE)AS.1943-5525.0000162.

Heiken, G. H., D. T. Vaniman, and B. M. French. (eds.). 1991. *Lunar sourcebook: A user's guide to the moon.* Cambridge University Press.

Houston, W.N., and L.I. Namiq. 1971. Penetration resistance of lunar soils. *Journal of Terramechanics* 8 (1): 59–69. https://doi.org/10.1016/0022-4898(71)90076-0.

Jaffe, L.D. 1971. Bearing strength of lunar soil. *The Moon* 3: 337–345.

Jiang, M., et al. 2017. 'DEM simulation of soil-tool interaction under extraterrestrial environmental effects. *Journal of Terramechanics: ISTVS* 71: 1–13. https://doi.org/10.1016/j.jterra.2017.01.002.

Jiang, M.J., H. Yu, and D. Harris. 2006. Discrete element modelling of deep penetration in granular soils. *International Journal for Numerical and Analytical Methods in Geomechanics* 30: 335–361. https://doi.org/10.1002/nag.473.

Johnson, J. B. 2003. A statistical micromechanical theory of cone penetration in granular materials cold regions research and engineering laboratory. CRREL Report, February.

Johnson, S. W., M. C. Koon, andW. D. I. Carrier. 1995. Lunar soil mechanics. *Journal of British Interplanetary Society*, 43–48.

Kirkham, M. B. 2014 *Penetrometers, principles of soil and plant water relations*. https://doi.org/10.1016/b978-0-12-420022-7.00011-2.

Kleinhenz, J. E., and R. A. Wilkinson. 2012. ISRU Soil mechanics vacuum facility: Soil bin preparation and simulant strength characterization. In *AIAA aerospace sciences meeting*, January, 1–8.

Kleinhenz, J. E., and R. A. Wilkinson. 2014. *Development and testing of an ISRU soil mechanics vacuum test facility*. Cleveland, Ohio.

Klosky, J.L., et al. 2000. Geotechnical behavior of JSC-1 lunar soil simulant. *Journal of Aerospace Engineering* 13 (4): 133–138. https://doi.org/10.1061/(ASCE)0893-1321(2000)13:4(133).

Kochan, H., et al. 1989. Crustal strength of different model comet materials. In *Physics and mechanics of cometary materials.*

Kuhn, M.R. 1987. *Micromechanical aspects of soil creep.* Berkeley: University of California.

Lacerda, W. A., and W. N. Houston. 1973. Stress relaxation in soils. In *Proceedings of the eighth annual conference on soil mechanics and foundation engineering,* Moscow, 221–227.

Leonovich, A.K., et al. 1971. Studies of lunar ground mechanical properties with the self-propelled Lunokhod-1. In *Peredvizhnaya Labotatoriya na Luna-Lunokhod-1*, 120–135. Moscow: Nauka.

Leonovich, A. K., et al. 1974. The main peculiarities of the processes of the deformation and destruction of lunar soil. In *The Soviet American conference on cosmochemistry of the moon and planets.* NASA SP-370.

Leonovich, A.K., et al. 1975. *Luna 16 and 20 investigations of the physical and mechanical properties of lunar soil.* Berlin: Akademie-Verlag.

Leonovich, A. K., et al. 1976. Investigation of the physical and mechanical properties of the lunar sample brought by Luna-20 and along the route of motion of Lunokhod 2. In *Proceedings of* *the XXIVth international astronautical congress,* Balu, USSR, 321–332. https://doi.org/10.1016/B978-0-08-020365-2.50031-7.

Li, Y., X. Zeng, and A. Wilkinson. 2013. Measurement of small cohesion of JSC-1A lunar Simulant. *Journal of Aerospace Engineering* 26 (October): 882–886. https://doi.org/10.1061/(ASCE)AS.1943-5525.0000197.

Liingaard, M., A. Augustesen, and P.V. Lade. 2004. Characterization of models for time-dependent behavior of soils. *International Journal of Geomechanics* 4 (3): 157–177. https://doi.org/10.1061/(ASCE)1532-3641(2004)4:3(157).

Lunne, T., P.K. Robertson, and J.J.M. Powell. 1997. *Cone penetration testing in geotechnical practice.* New York: Spon Press.

Mantovani, J. G., G. M. Galloway, and K. Zacny. 2016. Low force penetration of icy regolith. In *ASCE earth and space conference,* Orlando, FL.

McKay, D. S., et al. 1993. JSC-1: A new lunar regolith simulant. *Lunar and Planetary*, XXIV: 963–964.

Meyerhof, G. G. 1957. The ultimate bearing capacity of foundations on slopes. In *Proceedings of 4th ICSMFE,* London, England, 384–386.

Meyerhof, G.G. 1976. Bearing capacity and settlement of pile foundations. *Journal of the Geotechnical Engineering Division* 102 (3): 197–228.

Mitchell, J.K., et al. 1972. Mechanical properties of lunar soil: Density, porosity, cohesion, and angle of internal friction. *Proceedings of the Third Lunar Science Conference* 3: 3235–3253.

Mitchell, J. K., and S. Kenichi. 2005. Time effects on strength and deformation. *Fundamentals of Soil Behavior*, pp. 465–522.

Mulqueen, J., J.V. Stafford, and D.W. Tanner. 1977. Evaluation of penetrometers for measuring soil strength. *Journal of Terramechanics* 14 (3): 137–151.

Muthukumarappan, K., and G. J. Swamy. 2017. Rheology, microstructure, and functionality of cheese. In *Advances in food rheology and its applications,* ed. J. Ahmed, P. Ptaszek, and S. Basu, 245–276 Woodhead Publishing Series in Food Science, Technology and Nutrition. https://doi.org/10.1016/B978-0-08-100431-9.00010-3.

Oravec, H. A. 2009. Understanding mechanical behavior of lunar soils for the study of vehicle mobility, p. 662. https://doi.org/10.1061/40988(323)12.

Oravec, H.A., X. Zeng, and V.M. Asnani. 2010. Design and characterization of GRC-1: A soil for lunar terramechanics testing in Earth-ambient conditions. *Journal of Terramechanics. ISTVS* 47 (6): 361–377. https://doi.org/10.1016/j.jterra.2010.04.006.

Peleg, M., and M.D. Normand. 1983. Comparison of two methods for stress relaxation data presentation of solid foods. *Rheologica Acta* 22 (1): 108–113. https://doi.org/10.1007/BF01679835.

Perkins, S.W. 1991. *Modeling of regolith structure in extraterrestrial constructed facilities.* Boulder: University of Colorado.

Perkins, S.W., and C.R. Madson. 1996. Mechanical and load-settlement characteristics of two lunar soil simulants. *Journal of Aerospace Engineering* 9 (1): 1–9.

Pitcher, C., et al. 2016. Investigation of the properties of icy lunar polar regolith simulants. *Advances in Space Research* 57 (5): 1197–1208. https://doi.org/10.1016/j.asr.2015.12.030.

Puech, A., and P. Foray. 2002. Refined model for interpreting shallow penetration CPTs in sands. In *Proceedings of the annual offshore technology conference*, 2441–2449. https://doi.org/10.4043/14275-MS.

Rao, V.N.M., D.D. Hamann, and J.R. Hammerle. 1975. Stress analysis of a viscoelastic sphere subjected to temperature and moisture gradients. *Journal of Agricultural Engineering Research* 20 (3): 283–293. https://doi.org/10.1016/0021-8634(75)90064-5.

Ray, C. S., et al. 2010. JSC-1A lunar soil simulant: Characterization, glass formation, and selected glass properties. *Journal of Non-Crystalline Solids.* Elsevier B.V., 356(44–49): 2369–2374. https://doi.org/10.1016/j.jnoncrysol.2010.04.049.

Rohani, B., and G. Y. Baladi. 1981 *Correlation of mobility cone index with fundamental engineering properties of soil.*

Roylance, D. 2001. Engineering viscoelasticity, pp. 1–37.

Sanchez, P., and D. J. Scheeres. 2012. Cohesion in "Rubble-Pile" asteroids'. In *Asteroids, comets, meteors*.

Sanglerat, G. 1972. History of the penetrometer. In *The penetrometer and soil exploration: interpretation of penetration diagrams—Theory and practice*. Elsevier, pp. 1–91. https://doi.org/10.1016/B978-0-444-40976-8.50008-1.

Scott, R.F. 1987. Failure. *Geotechnique* 37: 423–466. https://doi.org/10.1680/geot.1987.37.4.423.

Seweryn, K., et al. 2014. Determining the geotechnical properties of planetary regolith using low velocity penetrometers. *Planetary and Space Science* 99: 70–83. https://doi.org/10.1016/j.pss.2014.05.004.

Sibille, L., et al. 2006. Lunar regolith simulant materials: Recommendations for standardization, production, and usage. In *NASA technical paper*, September 2006, 142. https://ntrs.nasa.gov/archive/nasa/casi.ntrs.nasa.gov/20060051776.pdf.

Snieder, R., C. Sens-Schönfelder, and R. Wu. 2017. The time dependence of rock healing as a universal relaxation process, a tutorial. *Geophysical Journal International* 208 (1): 1–9. https://doi.org/10.1093/gji/ggw377.

Stoeser, D., D. Rickman, and S. Wilson. 2010 *Design and specifications for the highland regolith prototype simulants NU-LHT-1M and -2M*.

Teale, R. 1965. The concept of specific energy in rock drilling. *International Journal of Rock Mechanics and Mining Science* 2 (1): 57–73.

Varney, A., et al. 2001. Prediction and interpretation of pore pressure dissipation for a tapered piezoprobe. *Géotechnique* 51 (7): 601–617. https://doi.org/10.1680/geot.2001.51.7.601.

Vesic, A.S. 1972. *Expansion of cavities in infinite soil mass*. Durham, NC: Duke University.

Willman, B.M., et al. 1995. Properties of lunar soil simulant JSC-1. *Journal of Aerospace Engineering* 8 (2): 77–87.

Wong, J.Y. 1989. *Terramechanics and off-road vehicles*. Amesterdam: Elsevier.

Yu, H.S., and J.K. Mitchell. 1998. Analysis of cone resistance: Review of methods. *Journal of Geotechnical and Geoenvironmental Engineering* 124 (2): 140–149. https://doi.org/10.1061/(ASCE)1090-0241(1998)124:2(140).

Zacny, K.A., et al. 2010. Robotic lunar geotechnical tool. *Earth and Space* 2010: 166–181.

Zeng, X., et al. 2010a. Geotechnical properties of JSC-1A lunar soil simulant. *Journal of Aerospace Engineering* 23 (April): 111–116. https://doi.org/10.1061/(ASCE)AS.1943-5525.0000014.

Zeng, X., C. He, and A. Wilkinson. 2010b. Geotechnical properties of NU-LHT-2M lunar highland simulant. *Journal of Aerospace Engineering* 23 (4): 213–218.